Noncollinear magnetism in liquid oxygen: A first-principles molecular dynamics study

Tatsuki Oda[1,3] and Alfredo Pasquarello[2,3]

[1]*Graduate School of Natural Science and Technology, Kanazawa University, Kanazawa 920-1192, Japan*
[2]*Institut de Théorie des Phénomènes Physiques (ITP), Ecole Polytechnique Fédéral de Lausanne (EPFL),
CH-1015 Lausanne, Switzerland*
[3]*Institut Romand de Recherche Numérique en Physique des Matériaux (IRRMA), CH-1015 Lausanne, Switzerland*

We perform first-principles molecular dynamics of liquid oxygen in which the magnetic structure evolves according to a generalized density-functional scheme allowing for noncollinear spin configurations. We investigate both structural correlations between the orientations of the molecular axes and magnetic correlations between the orientations of the molecular magnetic moments, demonstrating a clear relation between the local molecular configuration and the relative magnetic arrangement. The nuclear structure factor obtained from the simulation is found to agree well with the experimental one. The calculated magnetic structure factor shows antiferromagnetic correlations between molecules in the first shell, in accord with spin-polarized neutron scattering measurements. We observe the formation of dynamically coupled molecules, known as O_4 units, in which the molecular moments are aligned in an antiferromagnetic fashion. An analysis based on the life time of such units, revealed that in most cases the O_4 units occur as transient configurations during collisions. However, we also observed a small fraction of O_4 units surviving for relatively long periods. To account for electronic excitations which are missed in our density-functional scheme, we complement our description with a mean field model for the thermal fluctuations of the magnetic structure. The combined scheme is found to improve the description of the magnetic neutron structure factor and allows us to study the dependence of the magnetic susceptibility on temperature.

I. INTRODUCTION

The magnetic moment carried by the oxygen molecule is at the origin of many peculiar magnetic properties in both gaseous and condensed phases of oxygen. The low temperature crystal phases (the α, β, and γ-phases) are known to show antiferromagnetic correlations.[1] High-pressure phases have also been studied in connection with metallization, structural phase transition, and magnetism.[2–8] Unlike for crystalline phases, the lack of long-range order in gaseous and liquid phases prevents a direct analysis of the structural and magnetic properties. In particular, little is known so far about the way that different structural arrangements affect the local magnetism in such disordered forms of oxygen.

Extensive neutron diffraction experiments were carried out on liquid oxygen for characterizing the structural properties.[9,10] Henshaw was the first to obtain a neutron structure factor but was unable to separate out the magnetic and nuclear components.[9] Furthermore, the measured range of transferred momenta was insufficient for an accurate description in real space. Clarke *et al.* extended the measured range of transferred momenta using a pulsed neutron source.[11] The resulting radial distribution function shows both intra- and intermolecular correlations. Using a spin-polarized neutron scattering technique, Deraman *et al.* could separate out the magnetic component, revealing strong short-range antiferromagnetic correlations.[12]

In its ground state, the oxygen molecule is in a triplet spin state ($^3\Sigma_g^-$), corresponding to two unpaired electrons, coupled ferromagnetically according to Hund's rule. Liquid oxygen shows paramagnetic properties, with a magnetic susceptibility closely obeying a Curie-Weiss law.[13,14] This law typically describes magnetic systems of localized spins which interact only weakly with each other. The experimental data on liquid oxygen indicate that this interaction is antiferromagnetic.

However, a more careful analysis shows that the temperature dependence of the magnetic susceptibility of liquid oxygen cannot fully be described by a Curie-Weiss law.[1] The deviations result in a temperature dependent Weiss temperature, which could be explained by the formation of nonparamagnetic components in the liquid. The unpaired electrons in the ground state of the O_2 molecule could couple in a peculiar way to those of another nearby molecule,[15] leading to dimerization.[16] The dimerization of molecules in the liquid was postulated by Lewis[17] when analyzing the magnetic susceptibility.[13] Lewis modeled liquid oxygen as a mixture of O_2 and O_4 molecular units, treating them as paramagnetic and magnetically-saturated components, respectively.

The first definite evidence for the occurrence of O_4 molecules was provided by Long and Ewing, who found a relatively sharp absorption line on a broad collision-induced vibrational band in the infrared spectra of gaseous oxygen.[18] Since the absorption coefficient in this band varies proportionally to the square of the pressure, both features could be assigned to the dimerization of oxygen molecules.[19] Two kinds of dimerization were postulated, namely, the formation of long-living bound molecules and transient pairs of molecules formed during collision.[18] In their interpretation of the infrared and optical absorption spectra, Long and Ewing also suggested a floppy structure for the O_4 molecule, intermediate between the extreme cases of freely rotating and rigidly locked dimers.[18] In a later investigation of gaseous oxygen by quantum interference scattering, Aquilanti *et al.* further

analyzed the rotational and vibrational fine-structure of dimerized molecules.[16] This investigation gave access to the binding energy of the O_4 molecule and showed its dependence on the relative structural arrangement of the two oxygen molecules. A rectangular arrangement (H-type), in which the molecular axes of the two molecules are parallel, corresponding to a singlet spin state, was found to be the most stable form of the O_4 molecule. At variance with this detailed characterization of gaseous oxygen, the formation of oxygen dimers and their relative properties in the liquid state have remained far more elusive.

Recently, we reported in a concise form on an *ab initio* molecular dynamics investigation of liquid oxygen in which both the atomic structure and the noncollinear magnetic structure evolve without constraints.[20,21] We applied to liquid oxygen an electronic structure scheme which gives access to the noncollinear magnetic structure.[22] In this scheme, the direction and the magnitude of the magnetization are allowed to vary with position in real space. The treatment of the noncollinear magnetic structure appears crucial for a magnetic fluid like liquid oxygen. Indeed, in this liquid, the molecules carry individual magnetic moments, which interact with each other and may change their orientation during the diffusive motion. A particular interest in applying such a scheme to liquid oxygen resides in the possibility of highlighting the local correlations between the magnetism and the structural arrangement of molecules.

The investigation of liquid oxygen follows an application of this generalized electronic-structure scheme to small iron clusters, where it was used for performing a simultaneous relaxation of the atomic and magnetic degrees of freedom.[22] The work on liquid oxygen extends the application of this generalized scheme to molecular dynamics simulations.[20] The *ab initio* treatment of the noncollinear magnetic structure of an evolving fluid has remained a challenging task in atomic scale theory, and most investigations still focus on the magnetism of static configurations.[23–30] In our work, the calculated magnetic correlation function shows a good agreement with results from elastic neutron scattering.[20]

The present work complements our previous study in two ways. First, we provide a comprehensive account of our simulations on liquid oxygen, describing the underlying theory and giving a more complete analysis of our results. Second, we extend our previous study by a model theory for magnetic excitations, which were not considered in our previous investigation.[20] Inclusion of such excitations, brings the calculated magnetic structure factor in much closer agreement with experiment, further supporting the overall validity of our theory.

This paper is organized as follows: The generalized electronic-structure theory for the description of the noncollinear magnetism is briefly exposed in Sec. II. Section III contains details concerning the model system and the molecular dynamics simulation of liquid oxygen. Sections IV and V are devoted to the analyses of the atomic and magnetic structures, respectively. The dynamical properties of the O_4 molecular unit are analyzed in Sec. VI. Our results are summarized in Sec. VII.

II. THEORY FOR NONCOLLINEAR MAGNETIC STRUCTURES

In this section, we describe a scheme for treating noncollinear magnetic structures within electronic-structure calculations based on plane-wave basis sets and pseudopotentials.[22] In particular, the scheme is combined with molecular dynamics through the Car-Parrinello formulation.[31]

The noncollinear magnetic structure is represented by a vectorial spin density, $\mathbf{m}(\mathbf{r})$, which varies with position acting as a local magnetization density. The theoretical formulation is based on the introduction of a bispinor wave function Ψ for the Kohn-Sham orbitals:[32–34]

$$\Psi_i = \begin{pmatrix} \psi_{i1} \\ \psi_{i2} \end{pmatrix}, \qquad (1)$$

where the index i specifies the orbital among the set of Kohn-Sham orbitals $\{\Psi_i\}$. The electron density, $n(\mathbf{r})$, and the spin density, $\mathbf{m}(\mathbf{r})$, are found by expanding the density matrix, ρ, as follows:

$$\rho(\mathbf{r}) = \tfrac{1}{2}n(\mathbf{r})\sigma_0 + \tfrac{1}{2}[m_x(\mathbf{r})\sigma_x + m_y(\mathbf{r})\sigma_y + m_z(\mathbf{r})\sigma_z], \quad (2)$$

where σ_0 and σ_k $(k=x,y,z)$ are the unit and the Pauli spin matrices, respectively. The elements of the density matrix are given by

$$\rho_{\alpha\beta}(\mathbf{r}) = \sum_i^{\mathrm{occ.}} \{\psi_{i\alpha}(\mathbf{r})\psi_{i\beta}^*(\mathbf{r}) + \sum_{nmI} Q_{nm}^I(\mathbf{r})\langle\beta_n^I|\psi_{i\alpha}\rangle\langle\psi_{i\beta}|\beta_m^I\rangle\}, \tag{3}$$

where the second term in parentheses corresponds to a localized part of the electron density, which is peculiar to the ultrasoft pseudopotential scheme.[35,36] For each atom I, this term augments the electron density using localized charge density functions $Q_{nm}^I(\mathbf{r})$ and projector functions $\beta_n^I(\mathbf{r})$, centered at the nuclear position of the Ith atom.

In the local-axis representation, the spin density vector points along the z axis and the density reads:

$$U\rho U^\dagger = \begin{pmatrix} \tfrac{1}{2}n(\mathbf{r}) + \tfrac{1}{2}m(\mathbf{r}) & 0 \\ 0 & \tfrac{1}{2}n(\mathbf{r}) - \tfrac{1}{2}m(\mathbf{r}) \end{pmatrix}, \qquad (4)$$

where

$$m(\mathbf{r}) = [m_x^2(\mathbf{r}) + m_y^2(\mathbf{r}) + m_z^2(\mathbf{r})]^{1/2} \qquad (5)$$

and where $U(\theta,\phi)$ corresponds to the spin rotation matrix:

$$U[\theta(\mathbf{r}),\phi(\mathbf{r})] = \begin{pmatrix} e^{i\phi(\mathbf{r})/2}\cos[\theta(\mathbf{r})/2] & e^{-i\phi(\mathbf{r})/2}\sin[\theta(\mathbf{r})/2] \\ -e^{i\phi(\mathbf{r})/2}\sin[\theta(\mathbf{r})/2] & e^{-i\phi(\mathbf{r})/2}\cos[\theta(\mathbf{r})/2] \end{pmatrix}, \tag{6}$$

$$\sin\phi = -\frac{\mathrm{Im}\,\rho_{12}}{|\rho_{12}|}, \quad \cos\phi = \frac{\mathrm{Re}\,\rho_{12}}{|\rho_{12}|}, \qquad (7)$$

$$\sin\theta = \frac{2|\rho_{12}|}{m}, \quad \cos\theta = \frac{\rho_{11}-\rho_{22}}{m}. \tag{8}$$

We note that the matrix element ρ_{21} is given by the complex conjugate of ρ_{12} and that four real numbers are needed to represent the density matrix at a given point in real space. The present scheme does not impose any explicit condition on $\mathbf{m}(\mathbf{r})$, improving on earlier methods, in which atomic spheres were used with a uniform direction of the magnetization in each sphere.[33,37]

The Kohn-Sham energy of the system is given by

$$E_{\text{tot}}[\{\Psi_i\},\{\mathbf{R}_I\}] = \sum_i^{\text{occ.}} \langle\Psi_i| -\tfrac{1}{2}\nabla^2\sigma_0 |\Psi_i\rangle$$

$$+ \frac{1}{2}\int\int \frac{n(\mathbf{r})n(\mathbf{r}')}{|\mathbf{r}-\mathbf{r}'|}d\mathbf{r}d\mathbf{r}'$$

$$+ \int V_{\text{loc}}^{\text{ion}}(\mathbf{r})n(\mathbf{r})d\mathbf{r} + \sum_i^{\text{occ.}} \langle\Psi_i|V_{\text{NL}}|\Psi_i\rangle$$

$$+ E_{\text{xc}}[n,\mathbf{m}] + U_{\text{ion}}[\{\mathbf{R}_I\}], \tag{9}$$

where $\mathbf{R}_I$ represents the position of Ith atom, $V_{\text{loc}}^{\text{ion}}$ the local part of the pseudopotential, and U_{ion} the ion-ion interaction energy. The nonlocal part of the pseudopotential V_{NL} is given by

$$V_{\text{NL}} = \left(\sum_{nmI}|\beta_m^I\rangle D_{nm}^{(0)I}\langle\beta_n^I|\right)\sigma_0. \tag{10}$$

The quantities $\beta_n^I(\mathbf{r})$, $D_{nm}^{(0)I}$, $V_{\text{loc}}^{\text{ion}}(\mathbf{r})$, and $Q_{nm}^I(\mathbf{r})$ characterize the ultrasoft pseudopotential and are obtained from calculations for the isolated atom.[35]

Following the molecular dynamics scheme proposed by Car and Parrinello,[31] we construct a Lagrangian for both the electronic and atomic degrees of freedom:

$$\mathcal{L} = \sum_i^{\text{occ.}} m_\Psi \langle\dot\Psi_i|\dot\Psi_i\rangle + \frac{1}{2}\sum_I M_I\dot{\mathbf{R}}_I^2 - E_{\text{tot}}[\{\Psi_i\},\{\mathbf{R}_I\}]$$

$$+ \sum_{ij}^{\text{occ.}} \Lambda_{ij}(\langle\Psi_i|S|\Psi_j\rangle - \delta_{ij}), \tag{11}$$

where m_Ψ is the fictitious mass,[31] and M_I the mass of Ith atom. The last term in the Lagrangian corresponds to the orthonormal constraint for the wave functions and is here accounted for through the Lagrange multipliers Λ_{ij}. The overlap operator is given by $S=S_0\sigma_0$ and reads:

$$S_0 = 1 + \sum_{nmI} q_{nm}^I|\beta_m^I\rangle\langle\beta_n^I|, \tag{12}$$

where q_{nm}^I corresponds to the integral of the augmented charges:

$$q_{nm}^I = \int Q_{nm}^I(\mathbf{r})d\mathbf{r}. \tag{13}$$

The equations of motion for the various degrees of freedom are derived from the Euler-Lagrange equations:

$$m_\Psi\ddot\psi_{i\alpha} = -\frac{\delta E_{\text{tot}}}{\delta\psi_{i\alpha}^*} + \sum_j^{\text{occ.}} \Lambda_{ij}S_0\psi_{j\alpha} \equiv \xi_{i\alpha}, \tag{14}$$

$$M_I\ddot{\mathbf{R}}_I = -\frac{\partial E_{\text{tot}}}{\partial\mathbf{R}_I} + \sum_{ij}^{\text{occ.}} \Lambda_{ij}\langle\Psi_i|\frac{\partial S}{\partial\mathbf{R}_I}|\Psi_j\rangle \equiv \mathbf{F}_I, \tag{15}$$

where $\xi_{i\alpha}$ and $\mathbf{F}_I$ are the forces on the electronic and nuclear degrees of freedom, respectively, and their explicit expressions are given in Appendix A. We note that the two components of the spinor wave functions are only mixed by the force component deriving from the functional derivatives of E_{xc} with respect to the spin densities. This scheme provides the evolution of both the atomic trajectories and the spin density $\mathbf{m}(\mathbf{r})$.

III. SIMULATION

A. Model system and technical aspects

We modeled liquid oxygen using a periodic cubic cell of side 11.4 Å containing 32 independent molecules at the experimental density of 1.14 g/cm^3.[38] In our electronic-structure scheme, we used plane-wave basis sets in conjunction with ultrasoft pseudopotentials to describe core-valence interactions. Only the $1s$ states were included in the core, while the other states were described explicitly. The plane-wave basis sets are defined by energy cutoffs of 25 and 150 Ry for the electron wave functions and the electron density, respectively. The Brillouin zone of the simulation cell was sampled at the Γ point. In the construction of the ultrasoft pseudopotential, we used two reference energies, both for the $2s$ and $2p$ orbitals.

The exchange and correlation energy was treated within the generalized gradient approximation (GGA) proposed by Perdew and Wang (PW91).[39] In the calculation of the density gradient, we used $(U\rho U^\dagger)_{11}$ and $(U\rho U^\dagger)_{22}$ corresponding to the diagonal elements of the density matrix in the local-axis representation, and the resulting matrix for the exchange-correlation potential was regarded diagonal in the same representation.[40] In this treatment of the exchange-correlation energy, variations of the density gradient resulting from the spatial dependence of $\theta(\mathbf{r})$ and $\phi(\mathbf{r})$ are disregarded, and E_{xc} only depends on $n(\mathbf{r})$ and $m(\mathbf{r})$.[41]

With this setting for the electronic-structure calculations, we reproduced well the properties of the isolated oxygen molecule. The ground state corresponds to the spin-polarized state with a magnetization of $2\mu_B$ and shows a bond length of 1.25 Å, a vibrational frequency of 43.6 THz, and a binding energy of 5.84 eV, in fair agreement with the corresponding experimental values (1.21 Å, 47.39 THz, and 5.12 eV, respectively).[42] The energy gap in the O$_2$ molecule between the highest occupied and the lowest unoccupied states was found to be 2.4 eV. We define atomic magnetizations by integrating the spin density in atomic spheres with radii of 0.69 Å and obtained a value of 0.800 μ_B for each oxygen atom of the isolated O$_2$ molecule.

It is well known that density functional calculations employing the local density approximation (LDA) generally

lead to overbinding. In the GGA, this effect is reduced only in part. Our calculation gives a binding energy for the isolated oxygen molecule which overestimates the experimental value by 14%. We also performed a calculation to evaluate the binding energy of the antiferromagnetic arrangement of two oxygen molecules in the gaseous phase. Adopting the rectangular geometry at the experimental distance of 3.56 Å,[16] we found a binding energy of 19 meV, larger than the experimental one (17.1 meV) (Ref. 16) by 11%.

The molecular dynamics were started from an appropriate initial atomic configuration, in which intermolecular vibrations carried a random relative phase. The system first underwent a brief annealing cycle reaching temperatures of a few hundred Kelvin. Then, the temperature was fixed at T_{ex} $=90$ K by switching on thermostats.[43] At the temperature of T_{ex}, liquid oxygen lies close to the experimental liquid-vapor phase boundary.[38] The system was allowed to thermalize for a period of 5 ps. The subsequent evolution of 14 ps was used for calculating the physical quantities in this paper. We used a fictitious mass of $m_\Psi=200$ a.u. and a time step of 0.242 fs.

The computational cost of noncollinear magnetic structure calculations exceeds that of nonspin-polarized calculations by a factor which ranges between 10 and 20 depending on details of the system. Although the relative cost depends in practice on a combination of factors, the most important one results from the use of complex two-component spinor wave functions for every electron [Eq. (1)] rather than real single-component wave functions for every couple of electrons as in nonspin-polarized calculations. For instance, this difference leads to an increase of the computational load by a factor of 32 in the calculation of the overlap matrix for the orthonormalization of the wave functions and by a factor of 8 in the construction of the electron density by fast Fourier transformations. For our model system of liquid oxygen, we obtained a global factor of about 13.

B. Thermostats and total energy

In order to accelerate the instauration of an equilibrium state, we separately controlled the temperature of the three kinds of atomic motions, namely the translational, rotational, and vibrational motions. We thus introduced three Nosé thermostats,[44] defined by the Nosé variables, X_{tr}, X_{rt}, and X_{vb}, and obeying the following equations:

$$Q_{tr}\ddot{X}_{tr} = 2\left(K_{tr} - \tfrac{1}{2}g_{tr}k_B T_{ex}\right), \tag{16}$$

$$Q_{rt}\ddot{X}_{rt} = 2\left(K_{rt} - \tfrac{1}{2}g_{rt}k_B T_{ex}\right), \tag{17}$$

$$Q_{vb}\ddot{X}_{vb} = 2\left(K_{vb} - \tfrac{1}{2}g_{vb}k_B T_{ex}\right), \tag{18}$$

where g_{tr}, g_{rt}, g_{vb} are the numbers of degrees of freedom and K_{tr}, K_{rt}, K_{vb} are kinetic energies corresponding to each kind of atomic motion. The atomic positions then follow the equation:

$$\ddot{\mathbf{R}}_I = \mathbf{F}_I/M_I - \dot{X}_{tr}\dot{\mathbf{R}}_I^{tr} - \dot{X}_{rt}\dot{\mathbf{R}}_I^{rt} - \dot{X}_{vb}\dot{\mathbf{R}}_I^{vb}, \tag{19}$$

where $\dot{\mathbf{R}}_I^{tr}$, $\dot{\mathbf{R}}_I^{rt}$, and $\dot{\mathbf{R}}_I^{vb}$ are velocities corresponding to the respective kinds of atomic motion. In the simulation, the
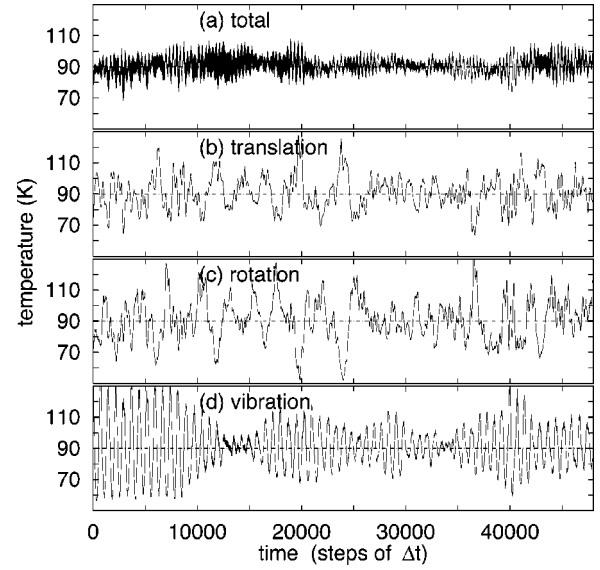

FIG. 1. Temperatures associated with the (a) full, (b) translational, (c) rotational, and (d) vibrational atomic dynamics. For the intramolecular vibrations in (d), the temperature results from a convolution which averages out fluctuations over a period of vibration. The horizontal lines indicate the imposed temperature of 90 K.

masses of the thermostats were taken to be $Q_{tr}=Q_{rt}=1$ $\times 10^6$ a.u. and $Q_{vb}=1\times 10^4$ a.u. These values were chosen sufficiently large to avoid that the thermalization frequencies of the thermostats interfered with the atomic dynamics. In addition, to prevent excitations of the electronic degrees of freedom, an electronic thermostat was applied according to the following equations:[43]

$$\ddot{\psi}_{i\alpha} = \xi_{i\alpha}/m_\Psi - \dot{x}_e\dot{\psi}_{i\alpha}, \tag{20}$$

$$\ddot{x}_e = 2(E_{kinc} - E_{kinc0})/Q_e, \tag{21}$$

where we used $Q_e=3\times 10^2$ a.u. and $E_{kinc0}=79$ meV. Through these thermostats, the temperatures associated to the three kinds of atomic motions could be maintained at T_{ex} during the course of the simulation, as illustrated in Fig. 1.

In a proper Car-Parrinello dynamics, the Kohn-Sham energy must not deviate significantly from the Born-Oppenheimer energy surface during the whole course of the simulation.[31] Without discontinuing the evolution, we examined the excitation with respect to the Born-Oppenheimer energy surface at several times during the simulation. We found an average excitation energy of 4.8 meV (0.35 mHa), with a maximal deviation of 10.2 meV (0.75 mHa). These energies are typically about an order of magnitude smaller than typical fluctuations of the Kohn-Sham energies (Fig. 2). In terms of temperature, the observed deviations correspond to ~1 K when compared to the typical fluctuations (~5 K) of the total atomic temperature.

C. Diffusion

To study the diffusion in our model system of liquid oxygen, we calculated the average mean square displacement (MSD) for atoms, given by
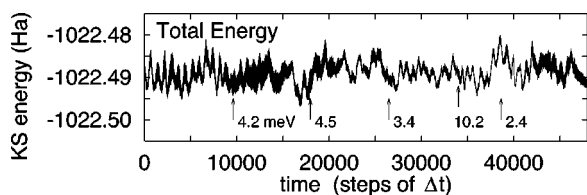
FIG. 2. Kohn-Sham energies in the molecular dynamics simulation. The numbers specify the deviations (in meV) from the Born-Oppenheimer energy surface.

$$\text{MSD} = \frac{1}{N} \sum_I \langle \{ \mathbf{R}_I(t+t') - \mathbf{R}_I(t') \}^2 \rangle_{t'}, \qquad (22)$$

where $\langle \; \rangle_{t'}$ indicates an average over initial time. Similarly, one obtains the analogous quantity for the diffusion of the centers of mass of the molecules. The diffusion shows standard liquidlike behavior, with both mean square displacements increasing linearly with time (Fig. 3). From the Einstein relation, $D = \lim_{t \to \infty} (\text{MSD})/6t$, we estimate a self-diffusion constant D of $2.3 \pm 0.2 \times 10^{-5}$ cm^2/s. This value is very similar to the tracer diffusion coefficient of ^{85}Kr (1.97×10^{-5} cm^2/s) in liquid oxygen at 88 K.[45]

D. Total magnetization

For a system with magnetic constituents, it is interesting to monitor the total magnetization $\mathbf{M}_{tot}$ in the unit cell. The typical time evolution of $\mathbf{M}_{tot}$ is shown in Fig. 4, where we did not apply any artificial rotation during the course of the simulation.[46] Each component of $\mathbf{M}_{tot}$ fluctuates around zero. For the time average of $\mathbf{M}_{tot}$, we obtained $\langle \mathbf{M}_{tot} \rangle = (-0.03, -0.03, 0.34)$ in units of μ_B per cell. Other averages gave $\langle |\mathbf{M}_{tot}| \rangle = 3.1 \; \mu_B$ and $\langle |\mathbf{M}_{tot}|^2 \rangle = 11.7 \; \mu_B^2$. These averages are all much smaller than the corresponding values for a hypothetical ferromagnetic alignment.

The fluctuating total magnetization is consistent with $\langle \mathbf{M}_{tot} \rangle = 0$, as appropriate for a paramagnetic fluid. At finite temperatures, a relation subsists between the average fluctuation of the magnetization and the magnetic susceptibility. However, our results cannot directly be connected to the sus-

FIG. 4. Total magnetization of our model system of liquid oxygen: (a) x, (b) y, and (c) z components, and (d) modulus.

ceptibility since the magnetization calculated in our simulation (Fig. 4) misses the contribution from electronic excitations. In fact, at any time, our simulation reproduced the system on the Born-Oppenheimer energy surface,[31] corresponding to the instantaneous ground state of the electronic system.

As the total magnetization fluctuates, the individual magnetic moments associated with the molecules rotate continuously covering all spatial directions in an essentially uniform way (not shown). During such rotations, the modulus of the atomic magnetizations shows very small fluctuations, indicating that the spin of each oxygen molecule is well preserved during the simulation. The distribution of calculated moduli is shown in Fig. 5. The distribution shows a peak with a slight tail for small values. The tail is explained by the observation that the molecular electronic state is perturbed during collisions, entailing a small reduction of the atomic magnetic moment (cf. Fig. 21 below). We found a mean value of $0.805 \; \mu_B$, almost the same as for the isolated O_2 molecule ($0.800 \; \mu_B$).
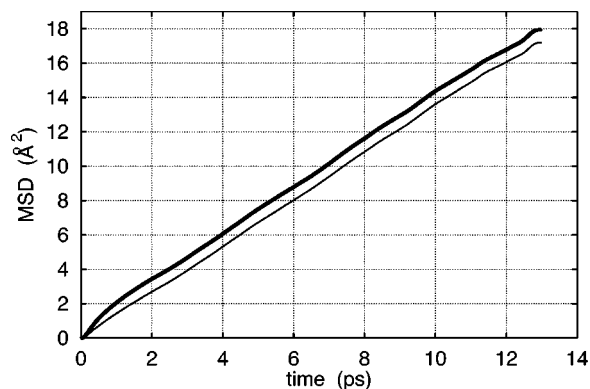

FIG. 3. Evolution of the mean square displacement (MSD) in our model system of liquid oxygen, for atoms (thick) and for molecular centers (thin).
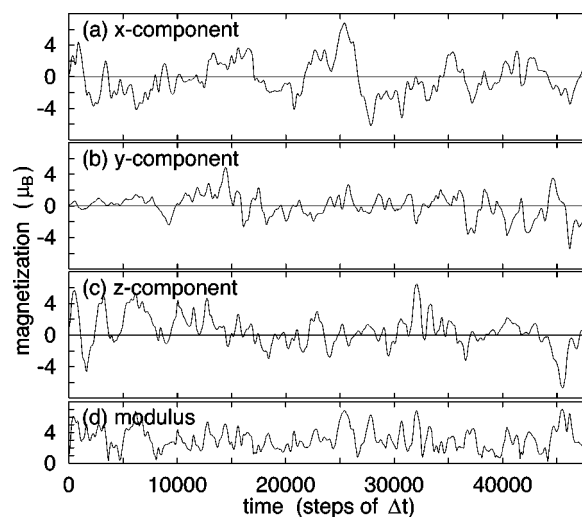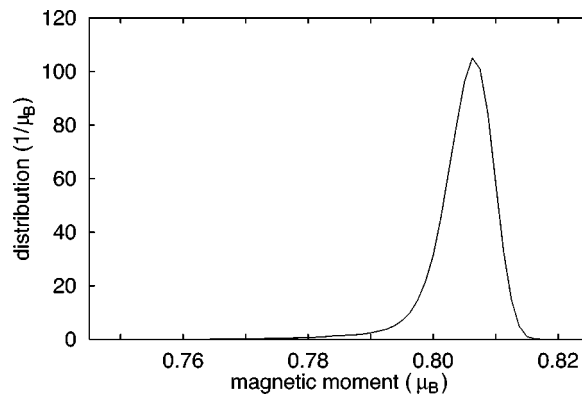

FIG. 5. Distribution of atomic magnetic moments as found during the simulation of liquid oxygen. We estimated atomic moments by integrating the spin densities within atomic spheres with radii of 0.69 Å. For comparison, the atomic moments for the isolated molecule are $0.800 \; \mu_B$.
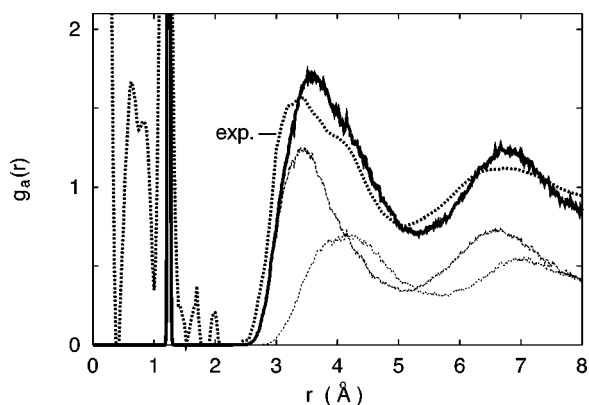
FIG. 6. Radial distribution functions for atoms $g_a(r)$ (solid), compared with the experimentally derived function (dotted) (Ref. 11). The two thin curves correspond to a decomposition separating the contributions from the closest and farthest O atom in each molecule.

Within the atomic region ($r_c \lesssim 0.69$ Å), the directions of the spin density $\mathbf{m}(\mathbf{r})$ are almost parallel to the averaged value, more than 99% of the grid points in the atomic sphere being aligned within 1° with respect to the averaged magnetization. The averaged atomic magnetization for one oxygen atom in a given molecule shows almost the same modulus and direction as that for the other oxygen atom in the same molecule. Maximum differences are 0.02 μ_B and 0.2° for modulus and direction, respectively. Consequently, the individual oxygen molecule in the liquid essentially preserves the magnetic properties of the isolated molecule.

IV. ATOMIC STRUCTURE

A. Radial distribution functions

The radial distribution function $g(r)$ provides orientationally averaged information about the structural arrangement of the particles:

$$g(r) = \frac{v_0 n(r)}{4\pi r^2}, \qquad (23)$$

where v_0 is the volume per particle and $n(r)dr$ represents the number of particles in the radial shell defined by the radii r and $r+dr$. Figures 6 and 7 show the radial distribution functions of atoms and molecules, $g_a(r)$ and $g_c(r)$. Including information derived from the corners of the simulation cell,[47] we investigated a radial range extending up to $\sqrt{2}L/2$ (~ 8 Å), where L is the side of the cubic cell. In Fig. 6, the sharp peak at 1.24 Å corresponds to the intramolecular structure. The distribution beyond 2.3 Å corresponds to intermolecular correlations, showing peaks at about 3.6 and 6.8 Å, separated by a minimum at 5.3 Å. All the main features in the calculated radial distribution function are also observed in the experimental function derived by Clarke *et al.*[11] In particular, the shoulder at about 4.1 Å is observed in both the calculated and experimental curves. This feature arises from second nearest atoms in neighboring molecules, as shown by the decomposition in Fig. 6.
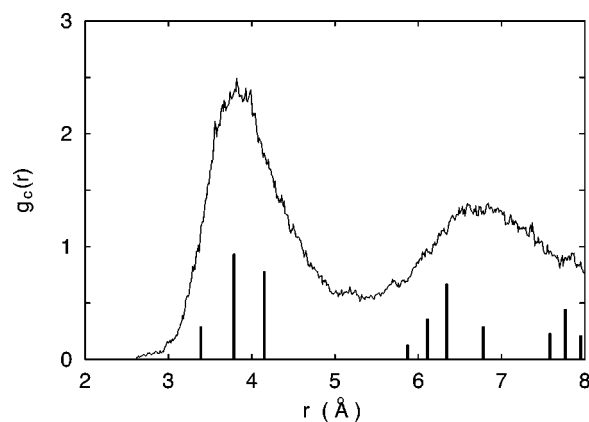

FIG. 7. Radial distribution function $g_c(r)$ for molecular centers. The vertical bars specify the distances and their associated weights for neighboring molecules in γ-O_2.

The radial distribution function for molecular centers $g_c(r)$ (Fig. 7) shows two peaks at 3.8 and 6.8 Å, separated by a minimum at 5.3 Å. The positions of the latter two features correspond to those in $g_a(r)$, thereby implying that orientational correlations are suppressed beyond the location of the first minimum. A comparison can be drawn between the structure in the liquid and that in the solid phase of γ-O_2.[1,48] The first shell of molecules in the liquid (until 5.3 Å) contains 13.0 molecules, quite close to the averaged number of molecules (13.5 molecules) occurring up to the third shell in γ-O_2. Furthermore, as shown in Fig. 7, the structural similarity is further supported by the overall shape of the distribution.

B. Nuclear structure factor

The structure factor $S(Q)$ is of interest because experimentally accessible by neutron diffraction measurements.[9–11] We calculated the structure factor as function of transferred momentum Q from the atomic configurations in our simulation as follows:

$$S(Q) = \frac{1}{N} \left\langle \left| \sum_I^N e^{-i\mathbf{Q}\cdot\mathbf{R}_I} \right|^2 \right\rangle, \qquad (24)$$

where N is number of atoms and $\langle \rangle$ represents a time average. The resulting structure factor is characterized by a sharp peak at about 2 Å^{-1}, a shoulder at 4 Å^{-1}, and a broader peak at 6 Å^{-1} (Fig. 8). The comparison between theory and experiment is overall very good, as shown in our previous work.[20]

The structure factor is connected to the radial distribution function $g_a(r)$ by Fourier transformation:

$$S(Q) = 1 + \frac{4\pi}{Q} \int_0^\infty \rho_{atm} g_a(r) r \sin(Qr) dr, \qquad (25)$$

where ρ_{atm} is the number density of atoms. This relation can be used to understand the origin of the peaks in the structure factor in terms of real-space correlations. The sharp peak in the structure factor results mainly from the diffraction due to
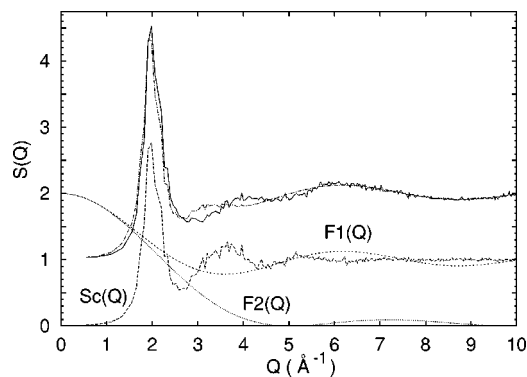
FIG. 8. Structure factor of liquid oxygen (solid) compared to the structure factor $S_{\text{uncorr}}(Q)$ derived in the approximation of uncorrelated orientations (dotted-dashed). For clarity, these structure factors are shifted by +1. The structure factor $S_{\text{uncorr}}(Q)$ is constructed from $F_1(Q)$ (short-dashed), $F_2(Q)$ (dotted), and $S_c(Q)$ (long-dashed) according to Eq. (26).

atoms belonging to different molecules, at the origin of the broad peak at 3.6 Å in $g_a(r)$ (Fig. 6). The oscillation in $S(Q)$ giving rise to the peak at 6 Å^{-1} arises from the intermolecular correlation at 1.24 Å in $g_a(r)$. Using relation (25), we could not so clearly identify the origin of the shoulder at 4 Å^{-1} in $S(Q)$. We show below that this feature results from a specific structural arrangement involving two molecules of the liquid.

C. Approximation of uncorrelated molecular orientations

To understand the structure of $S(Q)$ in greater detail, we considered the approximation by which the molecules in the liquid show statistically independent orientations. In this approximation, the structure factor becomes:[11]

$$S_{\text{uncorr}}(Q) = F_1(Q) + F_2(Q)[S_c(Q) - 1], \qquad (26)$$

where

$$S_c(Q) = \frac{2}{N}\left\langle \left| \sum_i^{N/2} e^{-i\mathbf{Q}\cdot\mathbf{r}_i} \right|^2 \right\rangle, \qquad (27)$$

$$F_1(Q) = \frac{1}{2}\left\langle \left| \sum_{I=1,2} e^{-i\mathbf{Q}\cdot\mathbf{R}_I} \right|^2 \right\rangle = 1 + j_0(Qd), \qquad (28)$$

$$F_2(Q) = \frac{1}{2}\left| \left\langle \sum_{I=1,2} e^{-i\mathbf{Q}\cdot\mathbf{R}_I} \right\rangle \right|^2 = 2[j_0(Qd/2)]^2, \qquad (29)$$

$$j_0(x) = \sin x / x. \qquad (30)$$

The structure factor $S_c(Q)$ in Eq. (27) is calculated from the molecular centers $\mathbf{r}_i$, specifying the position of the center of mass of the ith molecule. $F_1(Q)$ and $F_2(Q)$ are different molecular structure factors, both averaged over the molecular orientations. The parameter d represents the bond length of the molecule. Bond length fluctuations are neglected in this approximation, but would in any event not affect $S_{\text{uncorr}}(Q)$ significantly (cf. Fig. 10). We identify $F_2(Q)S_c(Q)$ with the

TABLE I. Definition of four order parameters specifying the relative orientation of two neighboring molecules. θ_1 and θ_2 give the polar angles between the respective molecular axes and the direction connecting the molecular centers. φ is the dihedral angle between the planes formed by the respective molecular axis and the axis connecting the molecular centers. The last column gives the spherical averages p_α^0 of the order parameters in the case of uncorrelated orientations.

Type	α	$p_\alpha(\theta_1, \theta_2, \varphi)$	p_α^0
H	a	$\sin^2\theta_1 \sin^2\theta_2 \cos^2\varphi$	0.222
X	b	$\sin^2\theta_1 \sin^2\theta_2 \sin^2\varphi$	0.222
T	c	$\sin^2\theta_1 \cos^2\theta_2 + \cos^2\theta_1 \sin^2\theta_2$	0.444
I	d	$\cos^2\theta_1 \cos^2\theta_2$	0.111

coherent part and $F_1(Q)-F_2(Q)$ with the incoherent part of the scattering. For simple atomic liquids ($d \to 0$), the incoherent scattering part vanishes. For a molecular liquid, however, there is an internal atomic structure in the molecules, which gives rise to the term $F_1(Q)-F_2(Q)$. The peak at 6 Å^{-1} in $S(Q)$ demonstratively shows the incoherent diffraction of the molecules. The derivation of the formulation for uncorrelated orientations is shortly reviewed in Appendix B.

In Fig. 8, we compare $S_{\text{uncorr}}(Q)$ with $S(Q)$. In the calculation of $S_{\text{uncorr}}(Q)$, we derived $S_c(Q)$ from the molecular centers in the simulation, and $F_1(Q)$ and $F_2(Q)$ from the bond length of the isolated molecule. The $S_{\text{uncorr}}(Q)$ is in good agreement with the $S(Q)$ for $Q < 2.5$ Å^{-1} and for $Q > 5$ Å^{-1}. In particular, it is interesting to focus on the peak at 2 Å^{-1}, which results from the first peak in $S_c(Q)$ and is therefore associated to the coherent scattering from different molecules. The good agreement between $S_{\text{uncorr}}(Q)$ and $S(Q)$ for this peak implies that this peak does not carry information on the relative orientations of neighboring molecules. In the intermediate range between 2.5 and 5 Å^{-1}, the $S_{\text{uncorr}}(Q)$ differs significantly from $S(Q)$, indicating that the approximation of uncorrelated orientations is only partially valid in liquid oxygen. In particular, the shoulder at 4 Å^{-1} in $S(Q)$ cannot be accounted for in this approximation.

D. Order parameters for local structure

To further examine the short-range molecular correlations, we defined four order parameters p_α describing the relative geometry of two molecules (cf. Table I). In Fig. 9, we report the order parameters as a function of distance between the molecular centers, averaged over the configurations in our simulation of liquid oxygen:

$$\langle p_\alpha \rangle / p_\alpha^0 = \frac{\left\langle \sum_{ij}^{i \neq j} p_\alpha(\theta_1, \theta_2, \varphi)\delta(r - r_{ij}) \right\rangle}{p_\alpha^0 \left\langle \sum_{ij}^{i \neq j} \delta(r - r_{ij}) \right\rangle}, \qquad (31)$$

where $r_{ij} = |\mathbf{r}_i - \mathbf{r}_j|$. As shown in Fig. 9, the short-range correlations between two molecules are governed by H-type (rect-
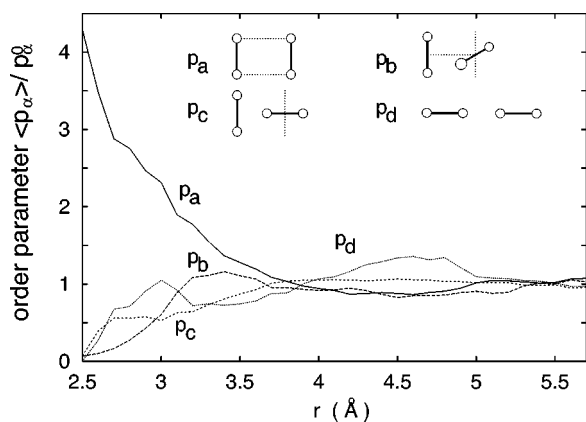
FIG. 9. Averaged order parameters as a function of distance between molecules. Their definition is given in the text. The ball and stick models represent the geometry maximizing the respective order parameter.

angular) configurations in which the molecular axes are parallel. This result indicates that the preferred correlations in the liquid correspond to those found both experimentally and theoretically in the gaseous phase.[16]

Inspired by the structure of solid γ-O_2,[1,48] Brodyanskii *et al.* suggested the formation of quasi-one-dimensional chains in liquid oxygen.[49] The short-range correlations found in H-type geometries can be regarded as the basic unit of such one-dimensional chains. Visual inspection of the molecular trajectories rules out the formation of longer molecular chains in our simulation.[50] However, our result cannot be definitive about the occurrence of longer chains in simulations with larger periodic cells or at lower temperatures.

E. Interpretation of nuclear structure factor

In order to analyze $S(Q)$ in terms of intermolecular correlations, we decomposed $S(Q)$ as follows:

$$S(Q) = 1 + S_{\text{intra}}(Q) + S_{\text{inter}}(Q), \tag{32}$$

$$S_{\text{intra}}(Q) = \frac{2}{N} \left\langle \sum_{\langle IJ \rangle}^{I \neq J(\text{intra})} \cos\{\mathbf{Q} \cdot \mathbf{R}_{IJ}\} \right\rangle, \tag{33}$$

$$S_{\text{inter}}(Q) = \frac{2}{N} \left\langle \sum_{\langle IJ \rangle}^{(\text{inter})} \cos\{\mathbf{Q} \cdot \mathbf{R}_{IJ}\} \right\rangle, \tag{34}$$

where $\mathbf{R}_{IJ} = \mathbf{R}_I - \mathbf{R}_J$ and the terms $S_{\text{intra}}(Q)$ and $S_{\text{inter}}(Q)$ result from intra- and intermolecular correlations, respectively. The term $S_{\text{intra}}(Q)$ includes the effect of bond length fluctuations, but, as shown in Fig. 10, agrees nonetheless very well with the corresponding quantity $F_1(Q) - 1$, in which these fluctuations are neglected (cf. Sec. IV C). The intermolecular term $S_{\text{inter}}(Q)$, also shown in Fig. 10, is characterized by two main peaks at 2 and 4 Å^{-1}, which correspond to well recognizable features in the total $S(Q)$ (Fig. 8).

To understand the origin of the peaks in $S_{\text{inter}}(Q)$ in terms of real-space contributions, we distinguish contributions to $S_{\text{inter}}(Q)$ according to the distance between molecular centers:
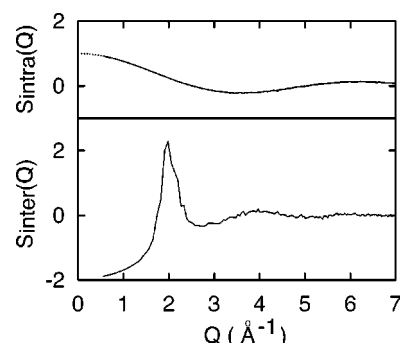

FIG. 10. Intra- and intermolecular contributions to the nuclear structure factor. Upper panel: $S_{\text{intra}}(Q)$ (full curve) and the function $F_1(Q) - 1$ (dotted curve). Lower panel: $S_{\text{inter}}(Q)$.

$$\begin{aligned}
S_{\text{inter}}(Q) = {} & \frac{2}{N} \left\langle \sum_{\langle IJ \rangle}^{r_{ij} < 3.8 \text{ Å}} \cos\{\mathbf{Q} \cdot \mathbf{R}_{IJ}\} \right\rangle \\
& + \frac{2}{N} \left\langle \sum_{\langle IJ \rangle}^{3.8 \leq r_{ij} < 5.3 \text{ Å}} \cos\{\mathbf{Q} \cdot \mathbf{R}_{IJ}\} \right\rangle \\
& + \frac{2}{N} \left\langle \sum_{\langle IJ \rangle}^{r_{ij} \geq 5.3 \text{ Å}} \cos\{\mathbf{Q} \cdot \mathbf{R}_{IJ}\} \right\rangle, \tag{35}
\end{aligned}$$

where the distances of 3.8 and 5.3 Å were chosen to correspond with the first peak and the first minimum in $g_c(r)$ (Fig. 7). Figure 11 shows that the three components in Eq. (35) all contribute to the sharp peak at 2 Å^{-1} in $S_{\text{inter}}(Q)$. It also appears clearly that the sharpness of this peak results from a remarkable cancellation between distance-dependent contributions.

It is also immediately clear from Fig. 11 that the peak at 4 Å^{-1} in $S_{\text{inter}}(Q)$ results from the diffraction of molecular pairs separated by less than 3.8 Å. We further analyzed the
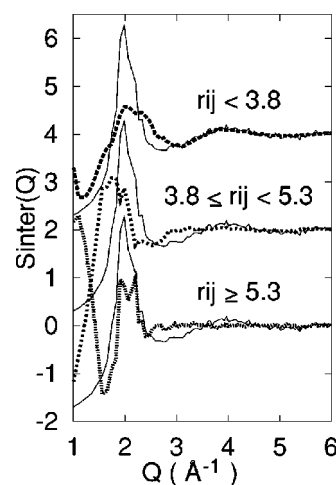

FIG. 11. Contributions to the intermolecular structure factor $S_{\text{inter}}(Q)$ distinguished on the basis of distance (r_{ij}) between scattering molecules: $r_{ij} < 3.8$ Å (upper broken), $3.8 \leq r_{ij} < 5.3$ Å (middle broken), $r_{ij} \geq 5.3$ Å (lower broken). The full $S_{\text{inter}}(Q)$ is shown for comparison (solid).
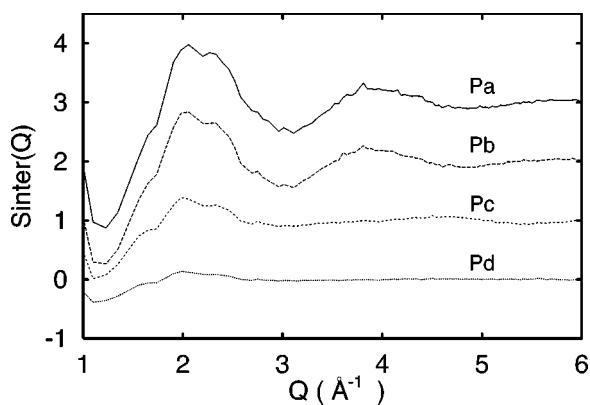
FIG. 12. Contributions to the intermolecular structure factor $S_{inter}(Q)$ resulting from molecules which are closer than 3.8 Å, further analyzed in terms of the order parameters, p_a, p_b, p_c, and p_d, from top to bottom.

contribution resulting from pairs of molecules with $r_{ij} < 3.8$ Å in terms of the order parameters p_α:

$$\frac{2}{N} \left\langle \sum_{\langle IJ \rangle}^{r_{ij} < 3.8 \text{ Å}} \frac{p_\alpha(\theta_1, \theta_2, \varphi)}{p_\alpha^0} \cos\{\mathbf{Q} \cdot \mathbf{R}_{IJ}\} \right\rangle. \qquad (36)$$

From the resulting four structure factors in Fig. 12, it is found that the H- and X-type geometries contribute to the peak at 4 Å^{-1}, while the T- and I-type geometries give vanishing contributions to this peak. Hence, we are able to conclude that the shoulder appearing at 4 Å^{-1} in the full $S(Q)$, which cannot be accounted for by the uncorrelated orientation model, indicates a predominance of H- and X-type molecular arrangements at distances smaller than 3.8 Å.

V. ELECTRONIC AND MAGNETIC STRUCTURES

A. Electronic density of states

Since the model system of liquid O_2 remained close to the Born-Oppenheimer energy surface during the course of the simulation, the electronic density of states (DOS) of liquid O_2 could be obtained from the Car-Parrinello eigenvalues, through diagonalization of the matrix Λ_{ij} in Eq. (14). Figure 13 gives the electronic DOS of liquid O_2 obtained as an average over an ensemble of configurations selected at equally separated intervals of 156 time steps.

We validated this procedure by considering the average DOS obtained for a limited set of configurations for which the electronic degrees of freedom were fully relaxed (cf. Sec. III). The fully relaxed eigenvalues were found to differ by at most 16 meV from those derived from the Λ_{ij} matrices for the same configurations, and the overall DOS associated to the occupied states is nearly indistinguishable from that obtained from an extensive average over Car-Parrinello eigenvalues (Fig. 13). This good agreement lends support to the density of unoccupied electronic states of liquid O_2 derived from the limited set of configurations for which the electronic structure was fully optimized. For comparison, we also report in Fig. 13 the calculated eigenvalues for the isolated O_2 molecule in its ground state.
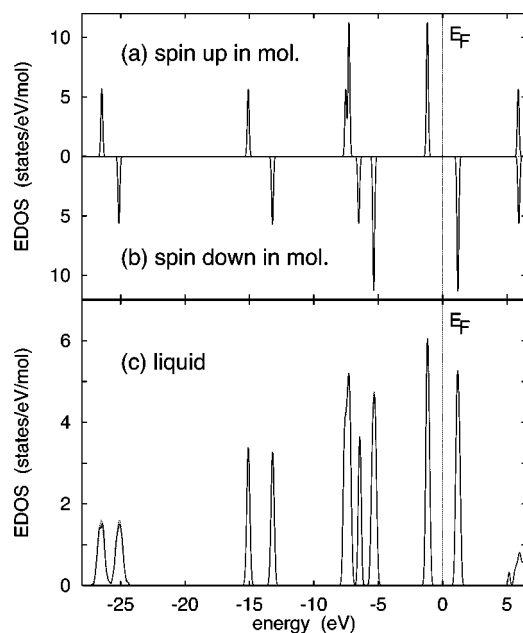

FIG. 13. Electron eigenvalues for (a) spin majority and (b) spin minority states of the isolated O_2 molecule in its ground state, compared to (c) the density of states of the liquid. For the liquid, the density of states is derived from both Car-Parrinello (dotted) and fully relaxed eigenvalues (solid). The energy levels were broadened with a Gaussian function with a width of 0.2 eV. The vertical line indicates the Fermi level.

The DOS of the liquid corresponds well to the eigenvalues of the isolated O_2 molecule. The condensation in the liquid state only associates a broadening to each eigenvalue. This broadening results primarily from thermally induced intramolecular vibrations, as revealed by electronic structure calculations for O_2 molecules with different bond lengths. This result is consistent with the observation that the largest broadening is observed for the deepest energy levels, associated to the σ-bonds of the 2s orbitals.

The exchange splitting in the isolated O_2 molecule gives rise to an energy gap of 2.4 eV between occupied and unoccupied energy levels. In the liquid, this energy gap is preserved. We estimate a gap of 1.9 eV, only slightly reduced with respect to that of the O_2 molecule. The reduction should be attributed to the broadening of the bands. In fact, the energy difference between the centers of the highest occupied and lowest unoccupied bands is found to be 2.4 eV, essentially unvaried with respect to the O_2 molecule. The persistence of an energy gap in the liquid state is related with the occurrence of a well defined magnetic state for each molecule. We note that our simulation indicates that the modulus of the molecular magnetization was found to show only a very small spread around its average value (Fig. 5).

B. Real space magnetic correlation

In order to study the magnetic structure, we introduce a magnetic correlation function in real space:

$$C(r) = \frac{\left\langle \sum_{ij}^{i \neq j} \mathbf{m}_i \cdot \mathbf{m}_j \delta(r - r_{ij}) \right\rangle}{\mu^2 \left\langle \sum_{ij}^{i \neq j} \delta(r - r_{ij}) \right\rangle}, \tag{37}$$

where $\mathbf{m}_i$ is the magnetic moment of the ith molecule and μ the average magnetic moment. For the molecular magnetic moment $\mathbf{m}_i$, we take the sum of the corresponding atomic moments, introduced in Sec. III D. The denominator in Eq. (37) is proportional to the radial distribution of molecular centers $g_c(r)$. The calculated correlation function $C(r)$ is shown in Fig. 14 (bottom panel). At short distances (until 4.4 Å), antiferromagnetic correlations prevail and grow with decreasing distance until they appear to saturate in the range 2.5–3.1 Å. At larger distances, the correlations are first ferromagnetic between 4.4 Å and 7 Å, and then again antiferromagnetic beyond 7 Å. At the position of the first peak in $g_c(r)$ ($r \sim 3.8$ Å), antiferromagnetic correlations dominate. Ferromagnetic correlations set in only at distances corresponding to the tail of the first peak in $g_c(r)$. In order to show the distribution of the magnetic correlations according to their statistical weight, we also give in Fig. 14 the magnetic radial distribution function $C(r)g_c(r)$. In this function, a peak corresponding to antiferromagnetic correlations occurs at 3.7 Å, essentially at the same position as the first peak in $g_c(r)$.

To understand the relation between magnetic and structural correlations, we weight the magnetic radial distribution function according to the order parameters p_α:

$$g_m^\alpha(r) \equiv \frac{\left\langle \sum_{ij}^{i \neq j} \mathbf{m}_i \cdot \mathbf{m}_j p_\alpha \delta(r - r_{ij}) \right\rangle}{\mu^2 p_\alpha^0 \left\langle \sum_{ij}^{i \neq j} \delta(r - r_{ij}) \right\rangle} g_c(r). \tag{38}$$

The resulting four functions are compared to the magnetic radial distribution function $C(r)g_c(r)$ in Fig. 14. At the shortest distances (2.5–3.1 Å), where a saturated antiferromagnetic alignment was observed in $C(r)$, the H-type geometry dominates. As the distance increases, the X-, T-, and I-type geometries intervene sequentially. Ferromagnetic alignment in the first neighbor shell is not favorable for any type of geometry and comes in at larger distances irrespective of geometry type.

The ferromagnetic alignment, observed in Fig. 14 for distances from 4.4 to 7.0 Å, is unlikely to result from a direct magnetic interaction because of the vanishingly small coupling calculated in Appendix C for such distances. More likely, the predominance of the antiferromagnetic interaction at short-range distances ($r = 2.5$–4.4 Å) causes ferromagnetic correlations between second nearest neighbors.

C. Magnetic structure factors

The magnetic structure factor has directly been measured by spin-polarized neutron diffraction and therefore constitutes an important experimental quantity with which the re-
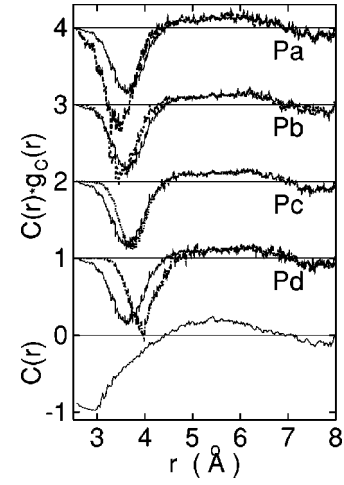

FIG. 14. Magnetic correlation function $C(r)$ (solid, lowest curve) and magnetic radial distribution function $C(r)g_c(r)$ (other solid curves). The broken curves correspond to magnetic radial distributions functions weighted according to the order parameters p_α: p_a, p_b, p_c, and p_d (see definition in text).

sults of our simulation should be compared. The magnetic structure factor $I(Q)$ is derived from the differential cross section and is associated to the spin density of the electrons:[12]

$$\frac{d\sigma}{d\Omega} = sI(Q), \tag{39}$$

$$I(Q) = \frac{2}{N\mu_0^2} \left\langle \left| \int d\mathbf{r} \, \mathbf{m}(\mathbf{r}) \exp(-i\mathbf{Q} \cdot \mathbf{r}) \right|^2 \right\rangle, \tag{40}$$

where μ_0^2 is the square of the molecular magnetic moment and s is the cross section of the isolated molecule:

$$s = s_0 \mathcal{S}(\mathcal{S} + 1)(g\mu_B)^2, \tag{41}$$

$$s_0 = 4.84 \times 10^{-2} (\text{b/sr} \cdot \mu_B^2). \tag{42}$$

In Eq. (41), we took a spin angular momentum $\mathcal{S} = 1$ (in units of $\hbar$) and a g-factor $g = 2$, as appropriate for the oxygen molecule.

We calculated the magnetic structure factor $I(Q)$ using the spin density $\mathbf{m}(\mathbf{r})$ associated to the valence wave functions in our simulation, the contribution from core electrons being negligible. As shown in Fig. 15, the calculated $I(Q)$ is characterized by a prominent peak at 1.2 Å^{-1} and a slight dip at 2 Å^{-1}.

Before addressing the comparison with experimental data, we first interpret the origin of the features appearing in $I(Q)$. To this end, it is particularly convenient to resort to an approximation of uncorrelated orientations of molecular moments, in a similar way as for the nuclear structure factor in Sec. IV C. The detailed derivation is given in Appendix B and gives:

$$I^{\text{uncorr}}(Q) = F_{m1}(Q) + F_{m2}(Q)[S_m(Q) - 1], \tag{43}$$
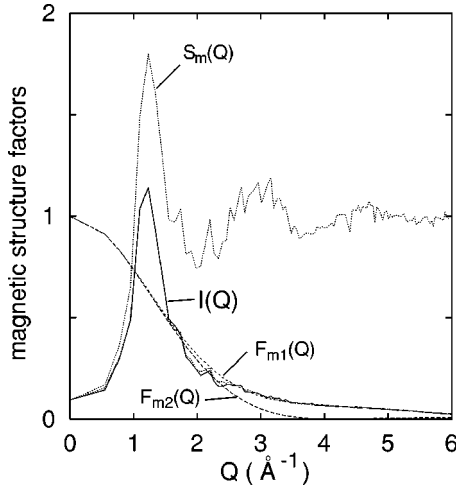
where

FIG. 15. Comparison between the magnetic structure factors $I(Q)$ (solid) and $I^{\text{uncorr}}(Q)$ (dotted). Note that $I(Q)$ and $I^{\text{uncorr}}(Q)$ barely differ from each other. Also shown are the structure factor of molecular magnetic moments $S_m(Q)$ and the molecular form factors F_{m1} and F_{m2}.

$$S_m(Q) = \frac{2}{N\mu^2}\left\langle\left|\sum_i \mathbf{m}_i e^{-i\mathbf{Q}\cdot\mathbf{r}_i}\right|^2\right\rangle, \tag{44}$$

$$F_{m1}(Q) = \langle|\mu(\mathbf{Q})|^2\rangle/\mu_0^2, \tag{45}$$

$$F_{m2}(Q) = |\langle\mu(\mathbf{Q})\rangle|^2/\mu_0^2. \tag{46}$$

The structure factor $S_m(Q)$ associated with the molecular magnetic moments is connected to the magnetic radial distribution function $C(r)g_c(r)$ by Fourier transformation:[12]

$$S_m(Q) = 1 + \frac{4\pi}{Q}\int_0^\infty \rho_{\text{mol}}C(r)g_c(r)r\sin(Qr)dr, \tag{47}$$

where ρ_{mol} is the number density of molecules. The orientationally averaged magnetic molecular form factors $F_{m1}(Q)$ and $F_{m2}(Q)$ are known as Kleiner factors,[51] and can be estimated from the Fourier transform $\mu(\mathbf{Q})$ of the spin density of the isolated O_2 molecule (cf. Appendix B). We note that, under the additional approximation of spherical spin density for the molecule, one derives $F_{m1}(Q)=F_{m2}(Q)$, which directly leads to the formula for $I(Q)$ given by Deraman *et al.*:[12] $I(Q)\simeq F_{m2}(Q)S_m(Q)$. However, we show below that this additional approximation does not account correctly for the behavior of $I(Q)$ at large values of Q.

The molecular form factors F_{m1} and F_{m2}, calculated in this work, are compared in Fig. 16 with the corresponding $\langle|f|^2\rangle$ and $|\langle f\rangle|^2$, originally derived by Kleiner from Mecklers' ground-state electronic wave function.[51] Although the overall shape is found to agree quite well, our form factors are found to be slightly larger than Kleiner's ones at least for small values of Q ($Q<6$ Å^{-1} for F_{m1} and $Q<4$ Å^{-1} for F_{m2}). We note that the Q values considered in Fig. 16 are sufficiently small to be well described within the pseudopotential framework adopted in our work.
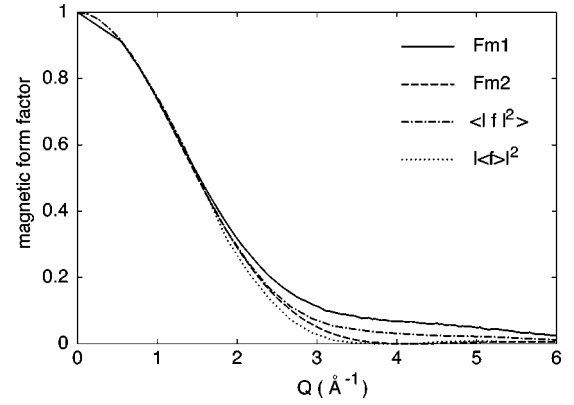

FIG. 16. Comparison between the orientationally averaged molecular magnetic form factors F_{m1} (solid) and F_{m2} (dashed) calculated in this work and the corresponding form factors $\langle|f|^2\rangle$ (dashed-dotted) and $|\langle f\rangle|^2$ (dotted) obtained by Kleiner (Ref. 51).

Figure 15 shows the comparison between $I(Q)$ and $I^{\text{uncorr}}(Q)$, along with the structure factors $S_m(Q)$, $F_{m1}(Q)$, and $F_{m2}(Q)$, which compose $I^{\text{uncorr}}(Q)$. The approximated $I^{\text{uncorr}}(Q)$ is found to reproduce $I(Q)$ extremely well. This indicates that it is possible to reconstruct the full spin density from the magnetic form factor $S_m(Q)$ and the orientations of the molecular magnetizations. Moreover, the good agreement with $I^{\text{uncorr}}(Q)$ provides a basis for interpreting the main features in $I(Q)$. The prominent peak at 1.2 Å^{-1} and the slight dip at 2 Å^{-1} are seen to originate from the oscillating shape of the magnetic structure factor $S_m(Q)$. At large values of Q (≥ 3.8 Å^{-1}), the fast decay of $F_{m2}(Q)$ causes $I(Q)$ to coincide with $F_{m1}(Q)$ [cf. Eq. (43)]. For vanishing Q, it is seen from Eq. (40) that $I(Q)$ is proportional to $\langle|\mathbf{M}_{\text{tot}}|^2\rangle$ and is therefore expected to vanish for a paramagnetic system. The finite value of $I(Q=0)$ in Fig. 15 only reflects a finite size error associated with the finite duration of our simulation.

Our analysis shows that the main features in $I(Q)$ relate with the magnetic structure factor $S_m(Q)$. It is therefore of interest to associate the structure in the latter function to real-space correlations. We decompose $S_m(Q)$ into different contributions pertaining to different distances between molecules:

$$S_m(Q) = 1 + \frac{2}{N\mu^2}\left\langle\sum_{ij(i\neq j)}^{r_{ij}<4.4\,\text{Å}}\mathbf{m}_i\cdot\mathbf{m}_j e^{-i\mathbf{Q}\cdot\mathbf{r}_{ij}}\right\rangle$$
$$+ \frac{2}{N\mu^2}\left\langle\sum_{ij(i\neq j)}^{4.4\leq r_{ij}<7.0\,\text{Å}}\mathbf{m}_i\cdot\mathbf{m}_j e^{-i\mathbf{Q}\cdot\mathbf{r}_{ij}}\right\rangle$$
$$+ \frac{2}{N\mu^2}\left\langle\sum_{ij(i\neq j)}^{r_{ij}\geq 7.0\,\text{Å}}\mathbf{m}_i\cdot\mathbf{m}_j e^{-i\mathbf{Q}\cdot\mathbf{r}_{ij}}\right\rangle, \tag{48}$$

where the limits at 4.4 and 7.0 Å were taken from the roots of $C(r)$. The resulting contributions are shown in Fig. 17. It clearly appears that the dip at 2 Å^{-1} results from the short-range antiferromagnetic correlations ($r<4.4$ Å). We verified that such a large dip is not formed when the sum is restricted to very small distances ($r<3.1$ Å), corresponding to satu-
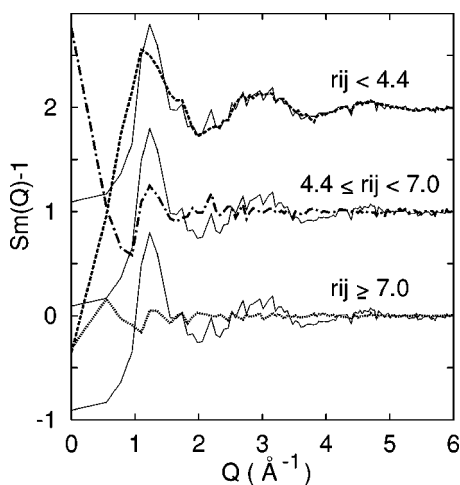
FIG. 17. Contributions to the magnetic structure factor $S_m(Q)$ -1 (solid) distinguished according to distance between molecules: $r_{ij} < 4.4$ Å (dashed), $4.4 \leqslant r_{ij} < 7.0$ Å (dashed-dotted), and $r_{ij} \geqslant 7.0$ Å (dotted).

rated antiferromagnetic correlations. From Fig. 17, it is also seen that the peak at 1.2 Å^{-1} results from both the antiferromagnetic $(r < 4.4$ Å) and ferromagnetic shells $(4.4 \leqslant r < 7$ Å).

The calculated $I(Q)$ is compared in Fig. 18 with experimental data from polarized neutron diffraction measurements.[12] Overall, the agreement between theory and experiment is fairly good. The dip at 2 Å^{-1} in the calculated $I(Q)$ reproduces the trend in the experimental data and the shoulder observed around $1-1.5$ Å^{-1} in the experiment corresponds well to the main peak in the calculated result. Furthermore, the tail at large values of Q values, which mainly results from the molecular form factor F_{m1}, agrees well with the experimental data. This agreement lends support to our F_{m1}, which showed significant differences with respect to Kleiner's $\langle |f|^2 \rangle$ for large Q values (Fig. 16).

Figure 18 also shows differences between the calculated and the experimental $I(Q)$. These concern the region of Q
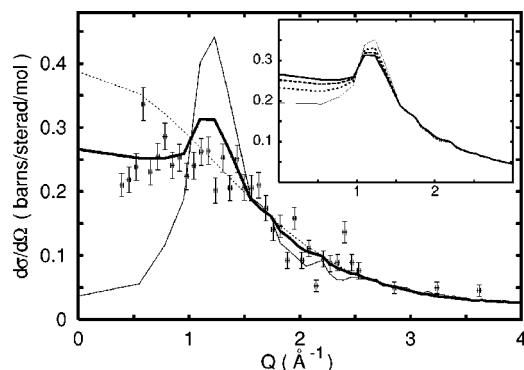

FIG. 18. Differential cross sections of elastic neutron scattering calculated with (thick) and without (thin) the finite temperature correction, compared with the experimental result of Deraman *et al.* (data with error bars) (Ref. 12). The thin dotted curve correspond to the molecular form factor $sF_{m1}(Q)$. Inset: Differential cross sections at temperatures of 90 K (thick solid), 82 K (thin dashed), 70.8 K (thin dotted), and 54 K (thin solid).

smaller than 1 Å^{-1} and the height of the main peak. Generally, the behavior at small Q values may be sensitive to long distance magnetic correlations, or thermal magnetic fluctuations. We attribute this difference to the fact that the magnetization $\mathbf{m}(\mathbf{r})$ derived from the wave functions in our simulations corresponds to the instantaneous electronic ground state, thereby missing contributions to the magnetization due to electronic excitations occurring at finite temperature (cf. Sec. III D). In the following section, we support this interpretation by accounting for these neglected contributions within a simplified scheme.

D. Thermal magnetic fluctuations

In our first-principles molecular dynamics simulation, the system evolved on the Born-Oppenheimer energy surface, thereby neglecting thermal electronic excitations.[31] To examine whether consideration of such excitations could affect the comparison between theory and experiment for the magnetic differential cross section, we developed a simplified model scheme. We described magnetic excitations within the Heisenberg model:

$$\mathcal{H} = \sum_{\langle ij \rangle} J_{ij} \mathbf{m}_i \cdot \mathbf{m}_j, \qquad (49)$$

where the sum is performed on nearest neighbor pairs and J_{ij} corresponds to the exchange interaction between the ith and jth molecules. For every atomic configuration, we assumed that the directions of magnetic moments $\{\mathbf{m}_i\}$ found in our *ab initio* molecular dynamics simulation correspond to the orientations of the magnetic ground state. The Heisenberg Hamiltonian then describes the thermal fluctuations with respect to the ground-state magnetic structure. Assuming a mean field approximation, the motion of each individual magnetic moment is governed by an effective magnetic field determined by the magnetic interactions with neighboring molecules. In this mean field approximation, Eq. (49) takes the form:

$$\mathcal{H} = -\sum_i h_i \cos \theta_i, \qquad (50)$$

where θ_i is the angle between the direction of the excited magnetic moment $\mathbf{m}_i$ and its ground-state orientation and h_i is proportional to the effective magnetic field acting on the ith molecule. The model can be simplified further. In consideration of the result in Fig. 5, we assumed rigid moduli for the magnetic moments and replaced these moduli by their average in the derivation of Eq. (50). To make possible a practical calculation, we further neglected the dependence of the effective magnetic field on the individual molecule. In this way, our model contains a single free parameter h corresponding to the average effective magnetic field acting on the molecules. We here used this energy scheme in a stochastic sampling procedure.

For a given atomic configuration, we sampled magnetic configurations at finite temperature using a Monte Carlo method and the Metropolis algorithm. This procedure is repeated for every atomic configuration retained from our *ab initio* molecular dynamics simulation (one out of every 1000
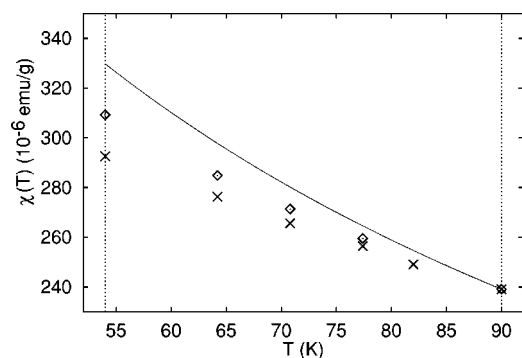
FIG. 19. Temperature dependence of the uniform magnetic susceptibility: present theory (crosses), experimental data from Ref. 13 (diamonds), and Curie-Weiss law with $\Theta = 41$ K (solid). The vertical lines indicate the boundaries of the liquid phase.

TABLE II. Temperature dependence of the thermodynamic quantities $I(0)$, $\chi(T)$, and $\Theta = T/I(0) - T$. Experimental data from Ref. 13 are given in parentheses.

T (K)	$I(0)$	$\chi(T)$ (10^{-6} emu/g)	Θ (K)
54	0.504 (0.533)	293 (309)	53.1 (47.3)
64.2	0.566 (0.584)	276 (285)	49.2 (45.8)
70.8	0.600 (0.613)	266 (271)	47.2 (44.7)
77.4	0.633 (0.641)	256 (260)	44.8 (43.3)
90	0.687 (0.687)	239 (239)	41.0 (41.0)

steps). The generated configurations were used for estimating $S_m(Q)$ in Eq. (44), and consequently $I^{uncorr}(Q)$ in Eq. (43). In this calculation, we fixed the mean field parameter h at 207 K,[52] so that the magnetic susceptibility derived from $I(0)$ at 90 K reproduced the experimental value.[13] The resulting magnetic differential cross section is shown in Fig. 18 for a temperature of $T = 90$ K. One notices that the account of thermal magnetic excitations noticeably improves the comparison with experiment, particularly at small values of Q. The theoretical peak at 1.2 Å^{-1} is now broadened and the dip with respect to the molecular form factor $F_{m1}(Q)$ occurring at 2 Å^{-1} suppressed.

Under the assumption that thermal effects due to electronic excitations dominate those associated to structural rearrangements, we studied the temperature dependence of $I(Q)$ using the structural configurations from our simulation. Our Monte Carlo calculations show that, with decreasing temperature, the main peak at 1.2 Å^{-1} becomes sharper and the value of $I(Q = 0)$ decreases (Fig. 18, inset). For a system of localized spins, the magnetic structure factor of $I(Q)$ in the thermodynamic limit $(Q \rightarrow 0)$ reads:

$$I(0) = 3k_B T \chi(T) / \mathcal{S}(\mathcal{S} + 1)(g\mu_B)^2, \quad (51)$$

where k_B is the Boltzmann constant and $\chi(T)$ the uniform isothermal magnetic susceptibility at the temperature T. Note that magnetic interactions between molecular magnetic moments and their thermal fluctuations are included in $\chi(T)$. In Fig. 19, we give the magnetic susceptibilities obtained within our model scheme for temperatures corresponding to the liquid phase. The results are also summarized in Table II. The calculated susceptibilities were found to increase with decreasing temperature in accord with the trend in the experimental data.[13] However, the variation in the theoretical data is not as pronounced as in the experiment.

It is convenient to interpret the magnetic susceptibilities in terms of the functional relation given by the Curie-Weiss law: $\chi(T) = C/(T + \Theta)$, where Θ is the Weiss temperature and C the Curie constant fixed at the theoretical value for noninteracting molecules, $C = N_m S(S+1)(g\mu_B)^2/3k_B$, N_m being the number of magnetic particles. The Weiss temperature generally represents the effective strength of the magnetic interac-

tion in a paramagnetic system of localized spins. Assuming a temperature-dependent Weiss temperature,[1] we found that the calculated susceptibilities are consistent with Θ varying from 53 K at $T = 54$ K to 41 K at $T = 90$ K (Table II), showing the same decreasing trend as the experimental data.[13]

As shown in Fig. 19, the magnetic susceptibilities vs temperature calculated within our simplified model scheme successfully reproduce the experimentally observed trend. However, the variation of the theoretical data is less pronounced, underestimating the experimental data by at most 5%. We note that this difference cannot be explained in terms of our neglecting the temperature dependence of the structure. In fact, the structure of the liquid at lower temperatures would favor the formation of antiferromagnetic configurations, thereby lowering the susceptibility even more. Overall, the achieved agreement does not represent a significant improvement with respect to the agreement $(+7\%)$ achieved by the Curie-Weiss law with a Weiss temperature chosen to reproduce the experimental susceptibility at 90 K (Fig. 19).

The effective mean field acting on each molecule was treated above as a free parameter. In Appendix C, we provide an order-of-magnitude estimate of this value based on the first-principles calculation of interactions between two molecules. This estimate gives a value of $h_{cal} = 132$ K, smaller by 36% with respect to the adopted value of h (207 K). The good agreement as far as the order of magnitude is concerned further supports the validity of the adopted model scheme. Our procedure for estimating h_{cal} also revealed that this parameter is sensitive to the amount of H-type correlations. This observation might provide a clue for improving the modeling of $\chi(T)$ beyond the simple scheme introduced in this work.

VI. DYNAMICAL PROPERTIES OF O$_4$ UNITS

A. Residence time

Although the diffusive behavior of liquid O$_2$ is trivial, the dynamics of the individual molecules is complicated by their molecular form and their magnetic interactions. The occurrence of correlations in the nuclear (Sec. IV) and magnetic structure factors (Sec. V) of the liquid suggest that the molecules show a tendency toward the formation of O$_4$ units.

To investigate the typical time scale associated to the formation of O$_4$ units, we turn to the scheme for estimating the average residence time introduced by Impey *et al.*.[53] Assuming a cutoff radius of $r_c = 3.1$ Å for defining colliding mol-
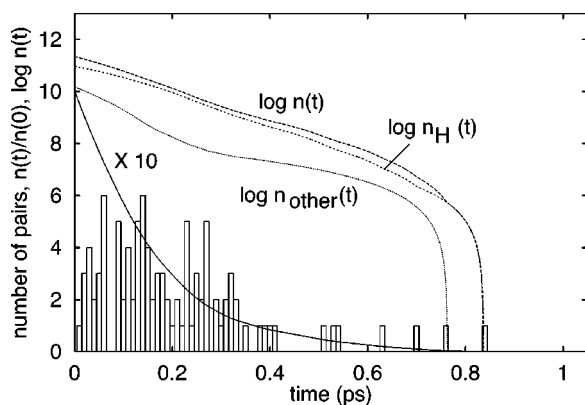
FIG. 20. Direct residence time (histogram) and time distribution functions $n(t)/n(0)$ (solid), $\log n(t)$ (long-dashed), $\log n_H(t)$ (short-dashed), and $\log n_{other}(t)$ (dotted).

ecules, we estimated the time distribution function $n(t)$ given by

$$n(t) = \sum_{t_n} \sum_{\langle ij \rangle}^{r_{ij} < r_c} P_{ij}(t_n, t), \qquad (52)$$

where $P_{ij}(t_n, t) = 1$ when the ith and jth molecules stay within a radius of r_c between the time steps t_n and $t_n + t$, and otherwise $P_{ij}(t_n, t) = 0$. The sum over t_n corresponds to sampling over a series of times in the simulation. Since $n(t)$ is generally found to decay exponentially, $n(t) = n(0)\exp(-t/\tau)$, we take its damping rate as definition of the average residence time τ. The curve for $\log n(t)$ in Fig. 20 indicates that the decay of $n(t)$ is indeed well represented by single exponent τ up to times of about 0.6 ps. From the slope of $\log n(t)$, we estimated a value of $\tau = 0.16$ ps. For comparison, we also evaluated the residence time directly by considering the time during which a pair of molecules remained within a distance determined by r_c. Figure 20 also shows the distribution of such direct residence times.

To examine whether the residence time depends on the relative geometric orientation of the colliding molecules, we distinguished molecular pairs using the order parameters p_a. Focusing on pairs for which $p_a > 0.8$, we calculated the corresponding time distribution function $n_H(t)$ and derived a residence time of $\tau_H = 0.20$ ps. This value of τ_H does not differ significantly from the residence time pertaining to the other colliding molecules, for which we found $\tau_{other} = 0.11$ ps. These results indicate that, although H-type geometries are dominant, the typical time scale of colliding molecules does not strongly depend on their relative geometrical arrangement.

B. Dynamics of long-living O_4 units

As one can see from the histogram in Fig. 20, there are several pairs of molecules forming O_4 complexes which survive for more than 0.6 ps. We illustrate the typical dynamical behavior of such O_4 units by reporting in Fig. 21 the time evolution of the structural parameters pertaining to a specific pair of molecules. The identified molecules approach very
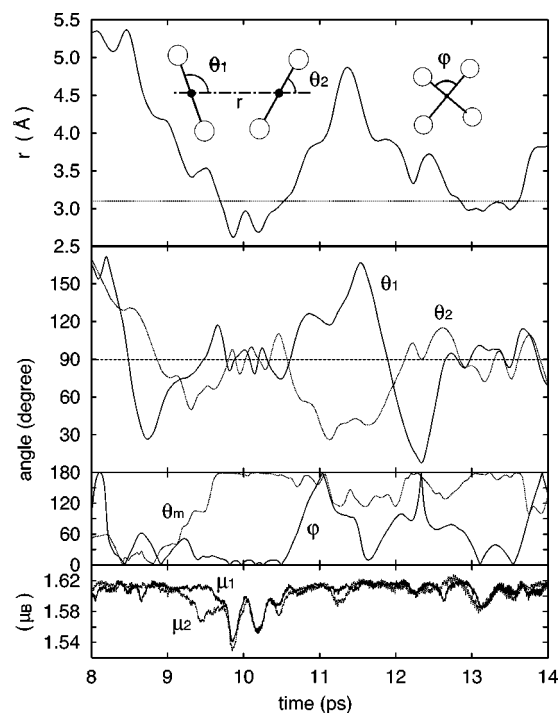

FIG. 21. Structural parameters vs time for a pair of molecules forming an O_4 unit. First panel: distance between molecules. Second panel: angles θ_1 and θ_2. Third panel: angle φ and angle (θ_m) between the orientations of the respective molecular magnetic moments. Fourth panel: magnitudes of the corresponding moments.

closely on two occasions in Fig. 21: at ~ 10 ps and at ~ 13 ps. On both occasions, the molecules assume an almost rectangular geometry ($\theta_1 = \theta_2 = 90°$ and $\varphi = 0$) and their molecular magnetic moments show an antiparallel alignment ($\theta_m = 180°$). During their approach at ~ 10 ps, the two molecules gently oscillate in antiphase around the rectangular geometry, suggesting that this configuration corresponds to a transient bonding state. Furthermore, the magnitudes of the molecular magnetic moments (μ_1 and μ_2) decrease, thereby implying that the electronic structure is subject to a perturbing interaction which delocalizes the spin density over the O_4 unit. The similar decrease of μ_2 at 9.5 ps (Fig. 21, fourth panel) corresponds to a close interaction with another nearby molecule. We note that when the molecules have moved away from each other, like for instance at ~ 11 ps, the antiferromagnetic alignment between their magnetic moments ($\theta_m \sim 180°$) may persist even up to relatively large distances (~ 4 Å). The second approach at ~ 13 ps shows a relatively weaker coupling, with larger oscillations in the structural angles and a smaller reduction of magnetic moments.

C. Discussion on the O_4 unit

In the simulation, the residence time for the most long-living pair of molecules is of 0.84 ps, five times longer than the average residence time for colliding molecules. As observed in Fig. 21, a long residence time appears to be associated with the formation of a quasistable O_4 unit. The num-

ber of pairs with residence times larger than 0.6 ps, which we identify as long-living pairs, is found to correspond to 4% of all the colliding pairs (cf. Fig. 20). From our simulation, we estimated that on average every molecule spends 1.4% of its time in a long-living pair.

Due to its linearly symmetric structure, an electric dipole transition associated with the excitation of a vibrational mode is not allowed for the isolated O_2 molecule. Therefore, the feature observed in the absorption spectra in correspondence of the vibrational frequency is most likely due to dimerization.[19] In fact, the intermolecular interaction giving rise to the O_4 unit breaks the linear symmetry and makes the electric dipole transition allowed. Under the assumption that the resulting transition probability is proportional to the residence time for every pair of colliding molecules, we estimate that the contribution from long-living pairs amounts to 18% of the total absorption coefficient. The fact that this value is noticeably larger than estimated for the gaseous phase ($\sim 2.5\%$) (Ref. 18) should be attributed to the higher density in the liquid.

The distance at which the antiferromagnetic correlation peaks in $C(r)g_c(r)$ (Fig. 14) does not differ significantly from the location of the first peak in $g_c(r)$ (Fig. 6). This property indicates a persistence of antiferromagnetic correlations even beyond the typical distances corresponding to the formation of the O_4 unit, as manifested by the slow decay of $C(r)$ between 3.1 and 4.4 Å. Our observations in Fig. 21 suggests that this property results from the preservation of an anti-alignment even after the collision, when the molecules are diffusing away.

When two molecules collide, it is difficult to predict whether the molecules would bounce off or form a long-living state. From our simulation, it appears that under particular circumstances, depending on the relative motion and the magnetic configuration, a pair of molecules can bind despite the thermal fluctuations and form a long-living quasi-stable O_4 unit. In this unit, the antiferromagnetic configuration corresponding to the rectangular H-type geometry enhances the attractive interaction between the molecules (cf. Appendix C). The occurrence of long-living O_4 units in our simulation implies that the energy gained by forming an O_4 unit should be comparable to the typical thermal energy k_BT. Hence, we expect that at temperatures lower than 90 K, the formation of O_4 units would be further favored. As the temperature of the liquid decreases, we therefore expect that the shoulder at 4 Å^{-1} in the structure factor $S(Q)$ should become more pronounced. It might also be possible that as the temperature drops, the enhanced stabilization of O_4 units could lead to chain-like structures as proposed by Brodyanskii *et al.* for the liquid[49] or observed in solid γ-O_2.

VII. CONCLUSION

We studied the noncollinear magnetic structure of liquid oxygen by carrying out *ab initio* molecular dynamics. In the simulation, both the atomic and magnetic structures were allowed to evolve according to density-functional equations for bispinor wave functions. The simulation was performed at a temperature of 90 K and spanned a time interval of

14 ps. The evolving system was maintained on the Born-Oppenheimer energy surface through the use of thermostats involving both nuclear and electronic degrees of freedom. Three nuclear Nosé thermostats acting on translational, rotational, and vibrational degrees of freedom were introduced to accelerate the thermal equilibration.

We studied the atomic structure of the liquid through radial distribution functions, nuclear structure factors, and local order parameters sensitive to the geometry of molecular pairs. The atomic radial distribution function and the nuclear structure factor were found in good agreement with corresponding results derived from experiment. It was found that the shoulder appearing in the main peak of the atomic radial distribution is originated from second-nearest neighbor atomic correlations resulting from first-neighbor molecules. The calculated nuclear structure factor reproduces all of the characteristic features observed in the experimental result. The main sharp peak at 2 Å^{-1} represents the coherent diffraction of neighboring molecules. The oscillating behavior giving rise to the broad peak at 6 Å^{-1} results from intramolecular diffraction. The shoulder at 4 Å^{-1}, which cannot be reproduced by a model assuming uncorrelated molecular orientations, is found to indicate specific molecular geometries of H- and X-type occurring at short distances ($r < 3.8$ Å). At distances shorter than 3.2 Å, the H-type geometry was found to dominate, while other geometries were all suppressed. The radial distribution of molecular centers is similar to that for solid γ-O_2, but visualization of the atomic trajectories did not show evidence for the formation of chain structures, as hypothesized in the literature.[49]

The electronic structure of liquid oxygen was not found to differ in any important aspect from that of the molecule in the gaseous phase. The main effects which were observed consist of a broadening of the energy levels. The preservation of the gap between occupied and empty electronic states ensures that each molecule could preserve its magnetization in the liquid. Collision between molecules caused slight perturbations in the electronic structure and were evidenced by a decrease of the molecular magnetizations.

The magnetic structure of the liquid shows properties typical of a system of localized spins. The molecular magnetizations show an almost constant modulus, with orientations pointing in all directions.

Magnetic correlation functions in real space and the magnetic structure factor were calculated from the magnetic configurations visited during our *ab initio* molecular dynamics. Both functions show antiferromagnetic correlations between molecular moments at short distances ($r < 4.4$ Å). In particular, we observed saturation in the magnetic correlations for distances smaller than 3.1 Å. We showed that the antiferromagnetic correlations are responsible for the peak at 1.2 Å^{-1} and for the dip at 2.0 Å^{-1} in the magnetic structure factor. These features find their origin in correlations in real space reaching up to 4.4 Å. At larger distances, ferromagnetic configurations prevail and were also found to contribute to the main peak in the magnetic structure factor. At short distances ($r < 3.1$ Å), structural and magnetic correlations were found to be highly synchronized, giving rise to colliding molecules forming a rectangular kind of geometry (H-type) and carrying antialigned magnetic moments.

In order to interpret the observed magnetic correlations, we introduced an approximation based on uncorrelated magnetic orientations. The magnetic structure factor calculated in this approximation was found to reproduce very accurately the magnetic structure factor calculated from the full spin density available in our *ab initio* molecular dynamics. The magnetic structure factor could directly be compared with experimental data from spin-polarized neutron diffraction measurements, showing a good correspondence for transferred momenta larger than 1.0 Å^{-1}. In particular, the correspondence between theory and experiment for the peak at 1.2 Å^{-1} and the dip 2.0 Å^{-1} support the occurrence of antiferromagnetic correlations in liquid oxygen. At small transferred momenta, the calculated cross section qualitatively differs from the experimental one. This is a consequence of the neglect of thermal magnetic excitations when evolving on the Born-Oppenheimer energy surface.

To verify the latter assertion, we studied thermal magnetic excitations within a mean field approximation. Accounting for such excitations, indeed brings calculated and measured magnetic structure factors in closer agreement. Within the adopted model, the magnetic structure factor accounts properly for the uniform thermal magnetic susceptibility in the thermodynamic limit and the main peak at 1.2 Å^{-1} broadens improving the agreement with the experimental data. Neglecting the dependence of the structure on temperature, we studied the thermal dependence of the magnetic susceptibility, finding agreement with the experimental trends. Similarly, the temperature dependence of the Weiss temperature agrees well with the trend derived from experimental susceptibilities.

By focusing on the time intervals during which molecular pairs remained within a cutoff distance of $r_c = 3.1$ Å, we derived a relatively short average residence time of 0.16 ps for colliding molecules. The averaged residence time was found to depend only weakly on the geometries of the colliding molecules. However, we also observed a small fraction of molecules evolving in quasistable bound states, for time intervals significantly longer than the average residence time.

In the present work, we set up an *ab initio* molecular dynamics scheme for studying the evolution of noncollinear magnetic structures. The application of this scheme to liquid oxygen allowed us to correlate atomic and magnetic structures during the simulation within a single theoretical framework based on first principles. The developed scheme provides a useful tool for studying correlations between magnetic and geometrical properties without assuming structures *a priori*.

ACKNOWLEDGMENTS

APPENDIX A: EXPRESSIONS OF FORCES

The explicit expression for the forces acting on the bispinor wave functions are given by

$$\Xi_i = \begin{pmatrix} \xi_{i1} \\ \xi_{i2} \end{pmatrix} = -H\Psi_i + \sum_j^{\text{occ.}} \Lambda_{ij} S\Psi_j, \tag{A1}$$

where,

$$H = \left(-\frac{1}{2}\nabla^2 \right)\sigma_0 + \bar{V}_{\text{eff}} + \sum_{nmI} |\beta_m^I\rangle \bar{D}_{nm}^I \langle \beta_n^I|, \tag{A2}$$

$$\bar{V}_{\text{eff}}(\mathbf{r}) = \left(V_{\text{loc}}(\mathbf{r}) + \int \frac{n(\mathbf{r}')}{|\mathbf{r} - \mathbf{r}'|} d\mathbf{r}' + V_{\text{xc}}^{\text{N}}(\mathbf{r}) \right)\sigma_0 + V_{\text{xc}}^{\text{M}}(\mathbf{r})\frac{\mathbf{m}(\mathbf{r}) \cdot \boldsymbol{\sigma}}{m(\mathbf{r})}, \tag{A3}$$

$$\bar{D}_{nm}^I = D_{nm}^{(0)I}\sigma_0 + \int Q_{nm}^I(\mathbf{r})\bar{V}_{\text{eff}}(\mathbf{r})d\mathbf{r}. \tag{A4}$$

Note that $\bar{V}_{\text{eff}}$ and $\bar{D}_{nm}^I$ are 2×2 matrices, and that $V_{\text{xc}}^{\text{N}}(\mathbf{r})$ and $V_{\text{xc}}^{\text{M}}(\mathbf{r})$ are defined by $\delta E_{\text{xc}}/\delta n(\mathbf{r})$ and $\delta E_{\text{xc}}/\delta m(\mathbf{r})$, respectively.

The atomic forces are given by

$$\mathbf{F}_I = -\sum_{\alpha\beta}\sum_{nm}(\bar{D}_{nm}^I)_{\alpha\beta}\frac{\partial \rho_{nm,\beta\alpha}^I}{\partial \mathbf{R}_I}$$
$$-\sum_{\alpha\beta}\int d\mathbf{r}[\bar{V}_{\text{eff}}(\mathbf{r})]_{\alpha\beta}\sum_{nm}\frac{dQ_{nm}^I(\mathbf{r})}{d\mathbf{R}_I}\rho_{nm,\beta\alpha}^I - \int d\mathbf{r}\frac{dV_{\text{loc}}^{\text{ion}}(\mathbf{r})}{d\mathbf{R}_I}$$
$$-\frac{dU_{\text{ion}}}{d\mathbf{R}_I} + \sum_{nm}\sum_\alpha q_{nm}^I\frac{\partial \omega_{nm,\alpha}^I}{\partial \mathbf{R}_I}, \tag{A5}$$

where

$$\rho_{nm,\alpha\beta}^I \equiv \sum_i^{\text{occ.}} \langle \beta_n^I|\psi_{i\alpha}\rangle\langle\psi_{i\beta}|\beta_m^I\rangle, \tag{A6}$$

$$\omega_{nm,\alpha}^I \equiv \sum_{ij}^{\text{occ.}} \Lambda_{ij}\langle\psi_{i\alpha}|\beta_m^I\rangle\langle\beta_n^I|\psi_{j\alpha}\rangle, \tag{A7}$$

$$\frac{\partial \rho_{nm,\alpha\beta}^I}{\partial \mathbf{R}_I} = \sum_i^{\text{occ.}}\left\{ \left\langle \frac{\partial \beta_n^I}{\partial \mathbf{R}_I}\Big|\psi_{i\alpha}\right\rangle\langle\psi_{i\beta}|\beta_m^I\rangle + \langle\beta_n^I|\psi_{i\alpha}\rangle \times \left\langle \psi_{i\beta}\Big|\frac{\partial \beta_m^I}{\partial \mathbf{R}_I}\right\rangle \right\}, \tag{A8}$$

$$\frac{\partial \omega_{nm,\alpha}^I}{\partial \mathbf{R}_I} = \sum_{ij}^{\text{occ.}}\Lambda_{ij}\left\{ \left\langle \psi_{i\alpha}\Big|\frac{\partial \beta_m^I}{\partial \mathbf{R}_I}\right\rangle\langle\beta_n^I|\psi_{j\alpha}\rangle + \langle\psi_{i\alpha}|\beta_m^I\rangle \times \left\langle \frac{\partial \beta_n^I}{\partial \mathbf{R}_I}\Big|\psi_{j\alpha}\right\rangle \right\}. \tag{A9}$$

APPENDIX B: FORMULATION FOR APPROXIMATION OF UNCORRELATED MOLECULAR ORIENTATIONS

We here shortly review the approximations of uncorrelated molecular orientations for nuclear and magnetic struc-

ture factors. We separate out from the nuclear structure factor $S(Q)$ the contribution coming from two different molecules:

$$\frac{1}{N}\sum_{ij}^{i\neq j}\sum_{\sigma,\tau=\pm 1}\langle e^{-i\mathbf{Q}\cdot\mathbf{r}_{ij}}e^{-i\mathbf{Q}\cdot(\sigma\mathbf{d}_i/2)}e^{-i\mathbf{Q}\cdot(\tau\mathbf{d}_j/2)}\rangle,\quad\text{(B1)}$$

where $\mathbf{r}_{ij}$ and $\mathbf{d}_i$ are vectors connecting the centers of the ith and jth molecules and the two atoms belonging to the ith molecule, respectively. Under the assumption that the orientations of $\mathbf{d}_i$ and $\mathbf{r}_{ij}$ are uncorrelated, we transform the contribution in Eq. (B1) to

$$\frac{1}{N}\sum_{ij}^{i\neq j}\sum_{\sigma,\tau=\pm 1}\langle e^{-i\mathbf{Q}\cdot\mathbf{r}_{ij}}\rangle\langle e^{-i\mathbf{Q}\cdot(\sigma\mathbf{d}_i/2)}\rangle\langle e^{-i\mathbf{Q}\cdot(\tau\mathbf{d}_j/2)}\rangle\quad\text{(B2)}$$

$$=\frac{2}{N}\left\langle\sum_{ij}^{i\neq j}e^{-i\mathbf{Q}\cdot\mathbf{r}_{ij}}\right\rangle\frac{1}{2}\left|\left\langle\sum_{\sigma=\pm 1}e^{-i\mathbf{Q}\cdot(\sigma\mathbf{d}/2)}\right\rangle\right|^2.\quad\text{(B3)}$$

In Eq. (B3), one recognizes that the first factor corresponds to $S_c(Q)-1$ and the second one to $F_2(Q)$. Upon an orientational average, the latter form factor only depends on the bond length (i.e., the modulus of $\mathbf{d}$). The contribution to $S(Q)$ coming from the intramolecular terms is nothing but $1+S_{\text{intra}}(Q)$ given in Eq. (32), which becomes $F_1(Q)$ under the additional assumption of constant bond length.

A similar approximation of uncorrelated orientations can be derived for the magnetic structure factor. We assume that the spin density can unambiguously be partitioned among the molecules. This is indeed the case in liquid oxygen, where the spin density is highly localized on the molecule. Furthermore, if we assume that the spin densities are uniform in each molecular region, we may consider the following decomposition:

$$\mathbf{m}(\mathbf{r})=\sum_i\mathbf{m}_i(\mathbf{r}-\mathbf{r}_i),\quad\text{(B4)}$$

and

$$\mathbf{m}_i(\mathbf{r})=\mu_i(\mathbf{r})\mathbf{e}_i,\quad\text{(B5)}$$

where $\mu_i(\mathbf{r})$ and $\mathbf{e}_i$ are the modulus and the unit vector associated to the magnetization of the ith molecule. Introducing the Fourier representation of $\mu_i(\mathbf{r})$,

$$\mu_i(\mathbf{Q})=\frac{1}{\Omega}\int d\mathbf{r}\,\mu_i(\mathbf{r})e^{-i\mathbf{Q}\cdot\mathbf{r}},\quad\text{(B6)}$$

where Ω is the volume of system, we can write the magnetic structure factor as follows:

$$I(Q)=\frac{2}{N\mu_0^2}\sum_i\langle|\mu_i(\mathbf{Q})|^2\rangle$$

$$+\frac{2}{N\mu_0^2}\sum_{ij}^{i\neq j}\langle\mu_i(\mathbf{Q})*\mu_j(\mathbf{Q})(\mathbf{e}_i\cdot\mathbf{e}_j)e^{-i\mathbf{Q}\cdot\mathbf{r}_{ij}}\rangle,\quad\text{(B7)}$$

where the two terms correspond to intra- and intermolecular contributions, respectively. For the latter term, we apply the approximation of uncorrelated molecular orientations in a similar way as for the nuclear structure factor. Decoupling

the molecular factor from the structure factor and neglecting the dependence of $\mu_i(\mathbf{Q})$ on the specific molecule, we finally obtain:

$$I(Q)\simeq\frac{1}{\mu_0^2}\langle|\mu(\mathbf{Q})|^2\rangle+\frac{1}{\mu_0^2}|\langle\mu(\mathbf{Q})\rangle|^2\frac{2}{N}\left\langle\sum_{ij}^{i\neq j}(\mathbf{e}_i\cdot\mathbf{e}_j)e^{-i\mathbf{Q}\cdot\mathbf{r}_{ij}}\right\rangle$$

$$\text{(B8)}$$

$$\cong F_{m1}(Q)+F_{m2}(Q)\frac{2}{N}\left\langle\sum_{ij}^{i\neq j}\frac{\mathbf{m}_i\cdot\mathbf{m}_j}{\mu^2}e^{-i\mathbf{Q}\cdot\mathbf{r}_{ij}}\right\rangle\quad\text{(B9)}$$

$$=F_{m1}(Q)+F_{m2}(Q)[S_m(Q)-1].\quad\text{(B10)}$$

In this derivation, we also assumed that $\mathbf{m}_i\cong\mu\mathbf{e}_i$, where μ is the average molecular magnetization.

It remains to be shown how we estimated $|\langle\mu(\mathbf{Q})\rangle|^2$ and $\langle|\mu(\mathbf{Q})|^2\rangle$, where the brackets $\langle\;\rangle$ represent a configurational average. For an isolated molecule this corresponds to an orientational average:

$$\langle f\rangle=\frac{\displaystyle\int f(\mathbf{Q})d\hat{\mathbf{Q}}}{\displaystyle\int d\hat{\mathbf{Q}}}=f(Q),\quad\text{(B11)}$$

where $d\hat{\mathbf{Q}}$ represents a differential solid angle associated to $\mathbf{Q}$. In this way, $F_{m1}(Q)$ and $F_{m2}(Q)$ are directly obtained from $\mu(\mathbf{Q})$ of the isolated O_2 molecule.

APPENDIX C: CALCULATION OF MEAN FIELD PARAMETER

We here provide a quantitative estimate of the mean field parameter which was fixed in the text through a comparison with the uniform magnetic susceptibility. By assuming a pairwise interaction, we estimated the mean field parameter as follows:

$$h_{\text{cal}}\simeq-\frac{2}{N}\left\langle\sum_{ij}^{i\neq j}J_{ij}\mathbf{m}_i\cdot\mathbf{m}_j\right\rangle$$

$$\simeq-\frac{4\pi}{v_m}\sum_\alpha p_\alpha^0\int_0^\infty\tilde{J}_\alpha(r)g_{\text{m}}^\alpha(r)r^2dr,\quad\text{(C1)}$$

where v_m is the volume per molecule, $\tilde{J}_\alpha(r)$ the exchange coupling energy associated to a geometry of type α, and $g_{\text{m}}^\alpha(r)$ the functions shown in Fig. 14. In the derivation of Eq. (C1), we used the approximation $\mu^2J_{ij}\simeq\Sigma_\alpha p_\alpha\tilde{J}_\alpha(r_{ij})$, where $\tilde{J}_\alpha$ corresponds to the exchange coupling energy in the geometry of type α. Since it is too complicated to extract $\tilde{J}_\alpha(r)$ from the simulation of the liquid, we here derive an estimate for $\tilde{J}_\alpha(r)$ by performing total-energy calculations for two interacting molecules in various geometries.

We derive the exchange coupling energy of $\tilde{J}_\alpha(r)$ from half the total-energy difference between the antiferromag-
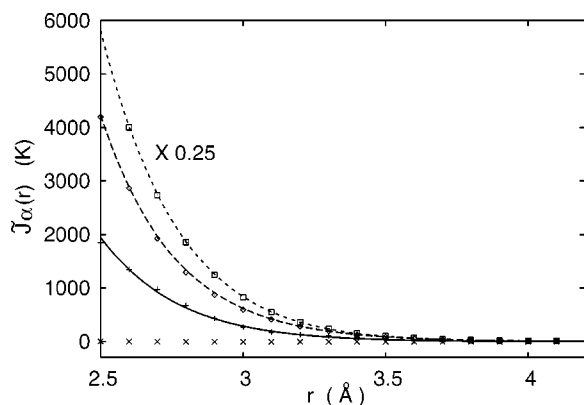
FIG. 22. Exchange coupling energies vs distance for four different geometries: $\tilde{J}_a(r)$ (solid, pluses), $\tilde{J}_b(r)$ (crosses), $\tilde{J}_c(r)$ (dashed, diamonds), and $\tilde{J}_d(r)$ (dotted, squares). The depicted values for $\tilde{J}_d(r)$ have been reduced to one-fourth of their calculated value for the purpose of illustration.

netic and ferromagnetic configurations of two molecules in a geometry of type α. Using our density functional approach, we calculated $\tilde{J}_\alpha(r)$ as a function of distance between the molecular centers (Fig. 22). For the H-, T-, and I-type geometries, it is convenient to parametrize the dependence of $\tilde{J}_\alpha(r)$ on distance using the functional form:[54]

$$\tilde{J}_\alpha(r) = \tilde{J}_\alpha(r_0)\exp[-A_\alpha(r - r_0) + B_\alpha(r - r_0)^2], \quad \text{(C2)}$$

where $r_0 = 3.2$ Å. The other parameters are given in Table III. For X-type geometries, the energy difference cannot be pa-

TABLE III. Exchange coupling energies at a distance of $r_0 = 3.2$ Å and the optimal values for the parametrized expression given in Eq. (C2).

Type	α	$\tilde{J}_\alpha(r_0)$ (K)	A_α (Å^{-1})	B_α (Å^{-2})
H	a	129	4.07	−0.27
X	b	−2.7		
T	c	286	3.86	−0.01
I	d	1454	4.27	−0.44

rametrized in the above form and takes on a small absolute value for any distance in Fig. 22. We note that our density-functional approach gives exchange coupling energies for the H-, T-, and I-type geometries, considerably larger than found in a previous Hartree-Fock calculation.[55]

Using Eq. (C1), we calculated a value of 132 K for h_{cal}. The H-, X-, T-, and I-type geometries are found to contribute to the calculated value of h_{cal} by 45%, −0.4%, 37%, and 19%, respectively. The negligible contribution from the X-type geometry results from the small values for $\tilde{J}_b(r)$ in Fig. 22. It is worth to note that the contribution from the H-type geometry is the largest one, although the corresponding exchange coupling energies are smaller than those of T- and I-type geometries. This is explained by the fact that the distribution function $g_m^a(r)$ corresponding to the H-type geometry shows a strong enhancement at short distances (Fig. 14).

[1] G. C. DeFotis, Phys. Rev. B **23**, 4714 (1981).

[2] Y. Akahama, H. Kawamura, D. Häusermann, M. Hanfland, and O. Shimomura, Phys. Rev. Lett. **74**, 4690 (1995).

[3] S. Serra, G. Chiarotti, S. Scandolo, and E. Tosatti, Phys. Rev. Lett. **80**, 5160 (1998).

[4] M. Otani, K. Yamaguchi, H. Miyagi, and N. Suzuki, J. Phys.: Condens. Matter **10**, 11 603 (1998).

[5] K. Kususe, Y. Hori, S. Suzuki, and K. Nakao, J. Phys. Soc. Jpn. **68**, 2692 (1999).

[6] F. A. Gorelli, L. Ulivi, M. Santoro, and R. Bini, Phys. Rev. B **63**, 104110 (2001).

[7] Y. Akahama, H. Kawamura, and O. Shimomura, Phys. Rev. B **64**, 054105 (2001).

[8] B. Militzer, F. Gygi, and G. Galli, Phys. Rev. Lett. **91**, 265503 (2003).

[9] D. G. Henshaw, Phys. Rev. **119**, 22 (1960).

[10] J. C. Dore, G. Walford, and D. I. Page, Mol. Phys. **29**, 565 (1975).

[11] J. H. Clarke, J. C. Dore, and R. N. Sinclair, Mol. Phys. **29**, 581 (1975).

[12] M. Deraman, J. C. Dore, and J. Schweizer, J. Magn. Magn. Mater. **50**, 178 (1985).

[13] A. Perrier and H. Kamerlingh Onnes, Phys. Comm. Leiden **139c-d**, 25 (1914).

[14] E. Kanda, T. Haseda, and A. Otsubo, Physica (Amsterdam) **20**, 131 (1954).

[15] L. Pauling, *The Nature of the Chemical Bond and the Structure of Molecules and Crystals: An Introduction to Modern Structural Chemisty* (Cornell University Press, New York, 1960), p. 353.

[16] Recently, the dimerization of oxygen has extensively been studied, mainly in the gaseous phase. See the following references and those cited therein: L. Biennier, D. Romanini, A. Kachanov, A. Campargue, B. Bussery-Honvault, and R. Bacis, J. Chem. Phys. **112**, 6309 (2000); V. Aquilanti, D. Ascenzi, M. Bartolomei, D. Cappelletti, S. Cavalli, M. D. C. Vitores, and F. Pirani, Phys. Rev. Lett. **82**, 69 (1999).

[17] G. N. Lewis, J. Am. Chem. Soc. **46**, 2027 (1924).

[18] C. A. Long and G. E. Ewing, Chem. Phys. Lett. **9**, 225 (1971); C. A. Long and G. E. Ewing, J. Chem. Phys. **58**, 4824 (1973).

[19] M. F. Crawford, H. L. Welsh, and J. L. Locke, Phys. Rev. **75**, 1607 (1949).

[20] T. Oda and A. Pasquarello, Phys. Rev. Lett. **89**, 197204 (2002).

[21] T. Oda and A. Pasquarello, J. Phys.: Condens. Matter **15**, S89 (2003).

[22] T. Oda, A. Pasquarello, and R. Car, Phys. Rev. Lett. **80**, 3622 (1998).

[23] L. Nordström and D. J. Singh, Phys. Rev. Lett. **76**, 4420 (1996).

[24] V. P. Antropov, B. N. Harmon, and A. N. Smirnov, J. Magn. Magn. Mater. **200**, 148 (1999).

[25] D. M. Bylander and L. Kleinman, Phys. Rev. B **59**, 6278 (1999).

[26] R. Gebauer, S. Serra, G. Chiarotti, S. Scandolo, S. Baroni, and E. Tosatti, Phys. Rev. B **61**, 6145 (2000).

[27] H. Yamagami, Phys. Rev. B **61**, 6246 (2000).

[28] K. Nakamura, A. J. Freeman, D. S. Wang, L. Zhong, and J. Fernandez-de-Castro, Phys. Rev. B **65**, 012402 (2001).

[29] D. Hobbs, G. Kresse, and J. Hafner, Phys. Rev. B **62**, 11 556 (2000).

[30] Ph. Kurz, F. Förster, L. Nordström, G. Bihlmayer, and S. Blügel, Phys. Rev. B **69**, 024415 (2004).

[31] R. Car and M. Parrinello, Phys. Rev. Lett. **55**, 2471 (1985).

[32] U. von Barth and L. Hedin, J. Phys. C **5**, 1629 (1972).

[33] J. Kübler, K. H. Höck, J. Sticht, and A. R. Williams, J. Phys. F: Met. Phys. **18**, 469 (1988).

[34] J. Kübler, *Theory of Itinerant Electron Magnetism* (Oxford University Press, New York, 2000), p. 56.

[35] D. Vanderbilt, Phys. Rev. B **41**, 7892 (1990).

[36] A. Pasquarello, K. Laasonen, R. Car, C. Lee, and D. Vanderbilt, Phys. Rev. Lett. **69**, 1982 (1992); K. Laasonen, A. Pasquarello, R. Car, C. Lee, and D. Vanderbilt, Phys. Rev. B **47**, 10 142 (1993).

[37] J. Sticht, K. H. Höck, and J. Kübler, J. Phys.: Condens. Matter **1**, 8155 (1998).

[38] *CRC Handbook of Chemistry and Physics*, edited by Robert C. Weast (CRC Press, Ohio, 1977), p. F-80.

[39] J. P. Perdew, J. A. Chevary, S. H. Vosko, K. A. Jackson, M. R. Pederson, D. J. Singh, and C. Fiolhais, Phys. Rev. B **46**, 6671 (1992).

[40] The same treatment has been found in K. Knöpfle, L. M. Sandratskii, and J. Kübler, Phys. Rev. B **62**, 5564 (2000).

[41] The diagonal elements of $U(\nabla\rho)U^{\dagger}$ represent the gradients of $(U\rho U^{\dagger})_{11}$ and $(U\rho U^{\dagger})_{22}$, which only contain $\nabla n(\mathbf{r})$ and $\nabla m(\mathbf{r})$. The off-diagonal elements of $U(\nabla\rho)U^{\dagger}$, for instance, $[U(\nabla\rho)U^{\dagger}]_{12} = \frac{1}{2}m(\mathbf{r})\nabla\theta(\mathbf{r}) + \frac{i}{2}m(\mathbf{r})\sin\theta(\mathbf{r})\nabla\phi(\mathbf{r})$, were not considered in the present formulation of the exchange-correlation functional.

[42] K. P. Huber and G. Herzberg, *Molecular Spectra and Molecular Structure: IV. Constants of Diatomic Molecules* (Van Nostrand Reinhold Company, New York, 1979), p. 490.

[43] P. E. Blöchl and M. Parrinello, Phys. Rev. B **45**, 9413 (1992).

[44] S. Nosé, Mol. Phys. **52**, 255 (1984); W. G. Hoover, Phys. Rev. A **31**, 1695 (1985).

[45] P. J. Dunlop and C. M. Bignell, J. Chem. Phys. **108**, 7301 (1998).

[46] Since our scheme neglects spin-orbit coupling, the orientation of the spin system remains unspecified by an undetermined global rotation. The indetermination in this rotation does not affect our results, except for the representation of the magnetization in Cartesian components in Figs. 4(a)–4(c). Furthermore, note that this condition restricts our investigation to relative orientations of local magnetizations at equal times.

[47] G. Galli and M. Parrinello, J. Chem. Phys. **95**, 7504 (1991).

[48] T. H. Jordan, W. E. Streib, H. W. Smith, and W. N. Lipscomb, Acta Crystallogr. **17**, 777 (1964).

[49] A. P. Brodyanskii, Yu. A. Freiman, and A. Jeżowski, J. Phys.: Condens. Matter **1**, 999 (1989).

[50] A video animation of our simulation is shown at http://cphys.s.kanazawa-u.ac.jp/˜oda/o2.html.

[51] W. H. Kleiner, Phys. Rev. **97**, 411 (1955).

[52] For each temperature, 5.6×10^5 configurations were used to estimate $I(Q)$. The acceptance ratio in the Metropolis algorithm varied between 30% and 50%, depending on temperature. An increase by a factor of 10 in the number of Monte Carlo steps led to a 0.1% variation of $I(0)$ at 54 K.

[53] R. W. Impey, P. A. Madden, and I. R. McDonald, J. Phys. Chem. **87**, 5071 (1983).

[54] M. Santoro, F. A. Gorelli, L. Ulivi, R. Bini, and H. J. Jodl, Phys. Rev. B **64**, 064428 (2001).

[55] M. C. van Hemert, P. E. S. Wormer, and A. van der Avoird, Phys. Rev. Lett. **51**, 1167 (1983).